

Design and Implementation of a Phased Array Antenna for Aviation

Burak Erdil Biçer*

**Department of Aeronautical Engineering, Istanbul Technical University*

I. Abstract

The design and realization of a phased array antenna system developed for aviation purposes are presented in this project. The proposed system is based on a 2x2 antenna array using patch antennas operating at 2.4 GHz. The study included a literature review, simulations using ANSYS HFSS and MATLAB, and the actual fabrication of patch antennas and phase shifting element interdigital capacitor (IDC). Vector network analyzer, PCB engraver and SDR were used to measure and realize designed antennas. The results obtained show the important contribution of phased arrays toward in the fields of communication, navigation, and safety within contemporary aerospace technology.

II. Introduction and Objectives

Systems of navigation and aviation communication have been transformed by phased array antennas. This was accomplished by means of fast and exact beam steering devoid of mechanical motion requirements. Originally designed for high-gain uses during World War Two, phased array antennas were developed. One of the applications of array antenna system used in the WWII is provided in the Fig. 1.

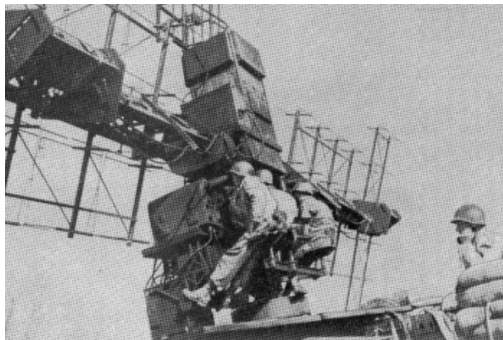


Figure 1: SCR-268 anti-aircraft tracking radar

However, since they can fit dynamic flight conditions and environmental constraints, they have become an indispensable component of contemporary aircraft technology. Phased arrays provide characteristics including multiple beam generating, adaptive beamforming, and wide-angle scanning, unlike conventional reflectors. These are absolutely necessary to improve radar systems and preserve consistent satellite communications [1]. Usage of phased array antenna can be observed in Fig. 2.

Phased array antennas play a crucial role in advancing aviation technologies across various applications. In air traffic control radar systems, these antennas provide high resolution 3D scanning in real time which is safer and more efficient for airport operations. Their capability to generate multiple beams simultaneously enhances surveillance and radar functionalities [2]. Moreover, phased arrays can be integrated into aircraft surfaces such as wings and fuselage panels to reduce drag. This also enhances the effectiveness of the intelligence and surveillance systems [3].

E-mail: *bicerb20@itu.edu.tr

Advisor: Asst. Prof. Ramazan Yeniçeri, Department of Aeronautical Engineering, Istanbul Technical University, yenicerir@itu.edu.tr



Figure 2: An example of phased array antenna used in the Mikoyan MiG-31 aircraft.

Furthermore, phased array antennas can be used to provide reliable high-speed data transmission. Ku-band phased arrays for communication between aircraft and ground stations provide this reliable transmission of data, contributing to modern communication infrastructure [4].

Essential parts of communication and radar systems are phase shifters. Using compact layouts and affordable PIN diodes, these allow exact electronic beam steering in phased array antennas including a high-pass/low-pass phase shifter operating in the ISM band. Thus, low power consumption and minimal phase errors can be obtained, which makes it perfect for modern transceivers requiring high precision and efficiency [5]. Furthermore, facilitating non-mechanical beam tilting in base transceiver station (BTS) antenna systems are passive phase shifters. Phase adjustments can be obtained with low cost by using dielectric materials such as alumina on microstrip transmission lines [6]. These cases highlight the adaptability and significance of phase shifters for enhancing system performance in several uses. Phase shifting results from changing the electromagnetic wave propagation speed. This process involves the dielectric constant of the substrate in great significance. Generally speaking, lower dielectric constant substrates are preferred since they help to reduce loss and improve radiation efficiency for use in radiation sources. To attain more tunability and phase control, phase shifters on the other hand need a higher dielectric constant. This contradictory need makes phase shifter and radiating element integration on a single substrate more difficult.

A ferroelectric material with a controllable dielectric constant is barium strontium titanate (BST). Therefore, exact phase control is achieved with BST rather often. Dynamic tuning of phase shifters is made possible by its ability to change permittivity under an applied electric field. In interdigital capacitors, BST can be used either as a filler or a substrate. BST provides non-linear tunability despite dynamic tuning capabilities, which presents design problems including impedance mismatches and higher reflection losses. By maximizing interdigital capacitor placement, which guarantees stability under different voltage conditions [7], these obstacles can be overcome. Although FR4 is often used as material in patch antennas, it is not usually fit for phase shifters. Its set dielectric constant is not tuned enough for dynamic phase control. Still, BST provides adjustable dielectric constants, which are better fit for phase shifter designs. Therefore, even with their cost efficiency, FR4's electrical characteristics restrict its effectiveness in phase shifters.

The basis of the phase shifter design is coplanar waveguides. Their planar construction lets phase shifting with passive components and simplifies fabrication. Adding capacitive loading by including interdigital capacitors into coplanar waveguides improves the phase-shifting capacity. Since their capacitance directly influences the propagation properties of the signal, interdigital capacitors are essential in obtaining the intended phase shift. By greatly enhancing the tunability and phase adjustment range, BST as the substrate for the interdigital capacitor gaps helps to enable exact control over beam steering in phased array systems. Phase shifters also have a naturally narrow band-width. Ultra-wide band systems that demand constant performance over a broad frequency range find this difficult. This constraint using continuously loaded coplanar waveguides. These designs together with BST's tunability offer a good way to integrate phase shifters with ultra-wide band phased arrays [7].

III. Methods and Resources

A. Methods Used in This Project

An extensive review of the literature helps one to start the development of a phased array antenna system for aviation uses. The emphasis of this review was on spotting and evaluating pertinent research and feasible designs. Articles including beam-steering methods, phase shifters, and phased array antenna designs were assessed closely. After the review of the literature, Ansys HFSS [8] and MATLAB [9] will be utilized. Simulations using high-fidelity electromagnetic simulations will use Ansys HFSS to allow exact analysis of antenna element performance, array configuration, and beam-steering capability. MATLAB will augment these initiatives using simulations run under the "Antenna Designer" and "PCB Patch Antenna Design Toolkit". MATLAB tools will enable effective design iterations and performance optimization of the patch antenna arrays. These center on reaching the intended frequency ranges and directional qualities.

We compare MATLAB's antenna toolbox's processing times and simulation features with Ansys HFSS. Rapid prototyping and iterative optimization of patch antenna arrays can benefit from MATLAB's "Antenna Designer" and "PCB Patch Antenna Design Toolbox." For similar designs, the HFSS and PCB Design Toolbox show similar processing times. MATLAB's Antenna Designer Toolbox is naturally slower in running simulations, though. While HFSS provides advanced capability for simulating complex electromagnetic environments, including structure-antenna simulations, MATLAB's antenna tools are limited to simulating basic antenna structures. Still, MATLAB offers a special benefit in including machine learning toolboxes into the design process. This capability enables creative ideas, such as using artificial intelligence to maximize antenna parameters which is not naturally supported in HFSS. The project will start the realization of the phased array antenna system after the simulation phase ends. This entails building the antenna elements and fittingly merging into the array construction. Careful testing of the physical implementation will help to validate the performance measures expected during the simulation period. From literature review to implementation, this iterative process guarantees a dependable phased array antenna design fit for contemporary aircraft systems.

B. Analysis of the Resources for This Project

The phased array antenna system for aviation uses must be realized successfully using modern tools and equipment. The building, testing, and validation of the intended system depend on these tools absolutely. This helps us to guarantee that the performance corresponds with the findings of simulation. This project depends mostly on a Vector Network Analyzer (VNA), a PCB engraver, and a Spectrum Analyzer (SA) or tools like Software-defined radio (SDR) to test and realize the necessary components.

Dimensions including return loss, transmission loss, and operating frequency of the constructed antenna array will be measured using the VNA. Validation of the simulation results and guarantees of operation within the desired frequency range depend on these measurements. The patch antenna will be created with a PCB engraver. This instrument guarantees great accuracy in the actual application of the simulated designs by allowing exact etching of the intended patterns onto the substrate. For this project, the PCB engraver is absolutely essential since it allows one to quickly prototype the antenna array and customize it. Particularly in regard to its spectral purity, power levels, and signal stability, the output of the phased array antenna system will be examined using the SDR. Evaluating the performance of the beam-steering mechanism and guaranteeing that the antenna system complies with the necessary aviation communication standards depend on this tool.

IV. Sections Specific to The Graduation Project

A. Building Blocks of Phased Array: Microstrip Patch Antennas

Microstrip patch antennas are essential components in modern communication systems. They are valued for their low-profile design, lightweight structure, and compatibility with planar and non-planar surfaces. These antennas consist of a thin metallic patch mounted on a grounded dielectric substrate. They radiate primarily through fringing fields at the edges of the patch, which makes them ideal for integration into devices such as mobile phones, satellites, and aerospace systems. The design of these antennas involves careful consideration of the patch dimensions, dielectric

substrate properties, and resonant frequency to achieve the desired performance [10]. Demonstration of a microstrip patch antenna is shown in Fig. 3.

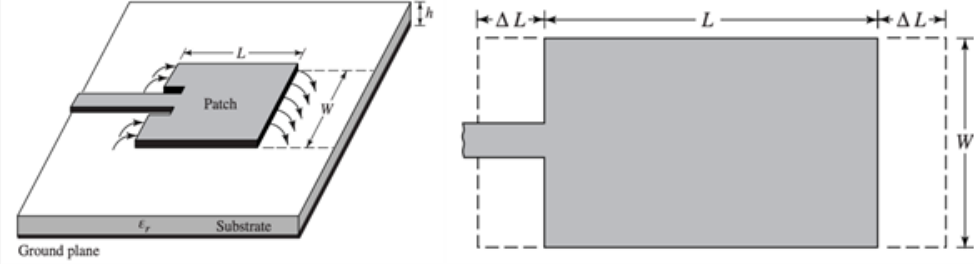


Figure 3: Edge-fed microstrip patch antenna [10]

The width of the patch is a critical parameter that influences the antenna's impedance and radiation efficiency. It is calculated based on the resonant frequency, the substrate's dielectric constant, and the speed of light. The relationship is given in the Eq. (1).

$$W = \frac{v_0}{2f_r} \sqrt{\frac{2}{\epsilon_r + 1}} \quad (1)$$

Whereas the dielectric constant controls the effective propagation of the electromagnetic waves inside the substrate. Eq. (1) guarantees that the width is proportional to the wavelength of the resonant frequency. Using the effective dielectric constant helps one to explain the interaction between the patch and the substrate: This parameter models the partial propagation of electromagnetic fields' effect on wave velocity in the dielectric substrate as well as in air. Computation of the effective dielectric constant it is done in Eq. (2).

$$\epsilon_{\text{eff}} = \frac{\epsilon_r + 1}{2} + \frac{\epsilon_r - 1}{2} \left[1 + 12 \frac{h}{W} \right]^{-1/2} \quad (2)$$

In Eq. (2), h represents the height of the dielectric substrate. A thicker substrate or a lower dielectric constant increases the effective wavelength. This improves the bandwidth but potentially reduces efficiency. The fringing effects, which occur due to the finite dimensions of the patch, extend the effective length of the patch. This extension is determined by the geometry of the patch and the effective dielectric constant, as described in the Eq (3).

$$\frac{\Delta L}{h} = 0.412 \frac{(\epsilon_{\text{eff}} + 0.3) \left(\frac{W}{h} + 0.264 \right)}{(\epsilon_{\text{eff}} - 0.258) \left(\frac{W}{h} + 0.8 \right)} \quad (3)$$

The extension modifies the resonant properties of the antenna and must be incorporated into the calculation of the patch's physical length. The actual patch length is then calculated to resonate at the desired frequency, taking into account the effective dielectric constant and the length extension as it can be observed in the Eq. (4).

$$L = \frac{v_0}{2f_r \sqrt{\epsilon_{\text{eff}}}} - 2\Delta L \quad (4)$$

Equation (4) guarantees correct phase velocity and radiation characteristics, so enabling the antenna to resonate at the designated frequency. While other dimensions fine-tune its impedance and bandwidth [10], the patch length mostly determines the fundamental resonant mode of the antenna. Important building blocks for phased array systems are microstrip patch antennas. By means of complex radiation patterns and beam-steering capability, these antennas can be configured in an array to improve their integration in advanced communication systems.

B. Coplanar Waveguides (CPW)

In microwave engineering, coplanar waveguides (CPWs) are extensively applied transmission line constructions. On the same substrate plane as can be seen in Fig. 4, a CPW comprises a central conductive strip flanked by two ground

planes. This planar architecture guarantees fit with integrated circuits, lowers radiation loss, and simplifies fabrication. Maintaining signal integrity in RF and microwave systems depends on precise control over impedance and efficient signal isolation made possible by CPW design. The dielectric properties of the substrate, signal line dimensions and signal line separation from the ground planes control the propagation characteristics of CPWs. Usually for most RF applications, these parameters are finely tuned to reach the desired impedance, typically 50 ohms. Flexible materials among other substrates allow CPWs to be integrated into contemporary, light-weight, small electronic systems.

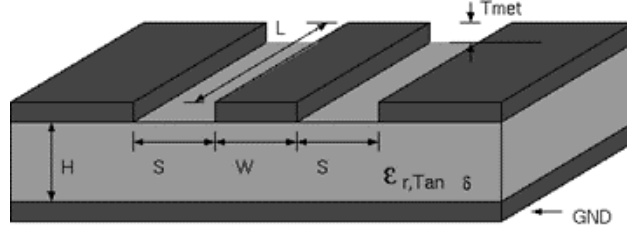


Figure 4: The structure of coplanar waveguide

CPWs form the fundamental transmission line structure in phase shifting systems. Capacitive or inductive loading elements allow one to change the phase velocity of electromagnetic waves spreading across the CPW. There is thus a controlled phase shift. For the development of adjustable and small-sized phase shifters, this quality makes CPWs perfect. One popular method is including interdigital capacitors into the CPW construction. As capacitive elements, IDCs control the transmission line's effective permittivity. Furthermore, the phase shift can be dynamically changed by using tuned dielectric materials such BST inside the IDC gaps. In phased array antennas, this allows exact control over beam steering, so improving their directional performance.

Phase shifters based on CPW can be classified according to loading configuration. Periodically loaded CPWs achieve a desired phase shift by using discrete capacitive or inductive elements along the transmission line. On the other hand, constantly loaded CPWs distribute tuning elements consistently over the transmission line. Because BST provides low loss tangent characteristics and high dielectric constant, both configurations can use it for tuning. A main difficulty in CPW phase shifter design is matching phase shift magnitude with insertion loss. Raising the line's capacitance improves the phase shift but also lowers impedance. This causes more reflection losses. Reducing these trade-offs by carefully arranging the tuning elements inside the CPW construction helps to optimize the dimensions. Integration of CPW to the phase shifting system is not utilized to the project since, for simplicity, substrate for RF components is chosen as FR4 and tunable phase shifting is not optimized for that substrate.

C. Interdigital Capacitors (IDC)

Designed to give exact capacitance within limited dimensions, interdigital capacitors (IDCs) are planar capacitive structures. As shown in Fig. 5, they comprise alternately conductive "fingers" on a dielectric substrate.

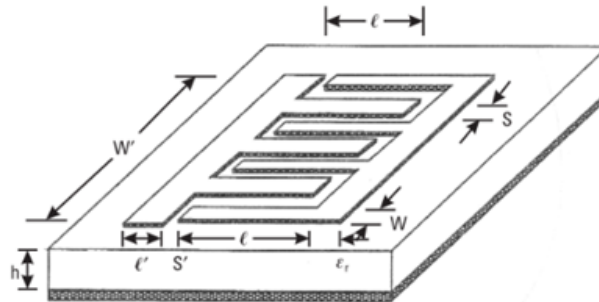


Figure 5: The structure of interdigital capacitor

The finger dimensions, the dielectric material properties, and the finger gap define the capacitance of an IDC. IDCs are extensively applied in high-frequency applications including filters, sensors, and phase shifters because of their

adjustable character. IDCs have a main advantage in design flexibility. By increasing the number of fingers or closing the distance between them, this adaptability lets engineers reach great capacitance with minimal space. Moreover, IDCs can be carried out on several substrates, including flexible materials or those having a strong dielectric constant.

Phase shifters in the framework of phased array antennas depend on IDCs as fundamental. By means of capacitive loading IDCs brought into the transmission path, one can modify the phase velocity. Phase shifters designed with IDCs present certain challenges. Reducing their gaps or adding more IDC fingers will help to increase capacitance and generate impedance mismatches and improved signal reflections. Moreover, phase shifters have a natural narrow-band character, thus it is sometimes difficult to guarantee a linear phase shift over a wide frequency range. Recent advancements using continuously loaded coplanar waveguides have showed that, provided design lowers impedance mismatches and maximizes phase shifting capability. Moreover, instead of serving as a substrate, BST applied to fill IDC gaps can improve tunability and reduce non-linearities. IDCs thus remain an essential technology in the development of phase shifters for phased array systems [7].

With the help of IDC structure, which combines capacitance, resistance, and inductance elements, interdigital capacitors behave as lumped RLC circuits. An RLC circuit has a phase given in Eq. (5).

$$\phi = \arctan\left(\frac{\omega L - \frac{1}{\omega C}}{R}\right) \quad (5)$$

The Fig. 6 indicates the RLC models of the interdigital capacitor at low and high frequencies. In part (a), the low-frequency model consists of a series combination of inductance, resistance, capacitance, and parasitic capacitance (C_s). This model is suitable for low-frequency applications. In part (b), the high-frequency model includes additional components such as inductance (L'), resistance (R'), and capacitance (C'), along with parasitic capacitances (C_{s1} , C_{s2} , C_{s3}). At high frequencies, these parasitics significantly affect the IDC's impedance and frequency response, which is crucial for high-frequency circuit design [11].

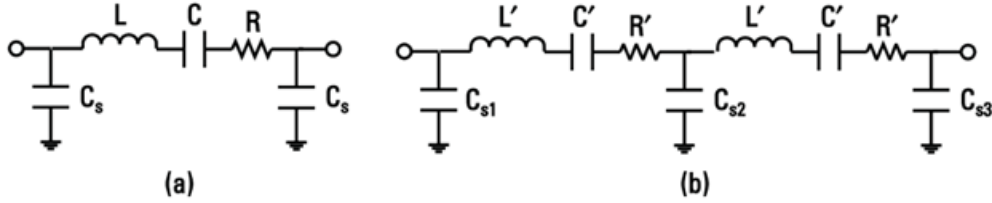


Figure 6: RLC models of the interdigital capacitor: (a) low frequency and (b) high frequency

In order to calculate the resistance value of the interdigital capacitor, the Eq. (6) can be used where R_s is the sheet resistivity, W is the width of the fingers, and N is the number of fingers.

$$R = \frac{4}{3} \times \frac{\ell}{W \times N} \times R_s \quad (6)$$

In order to calculate the inductance value of the interdigital capacitor, the Eq. (7) can be used, where Z_0 is the characteristic impedance and ϵ_{re} is the relative permittivity.

$$L = \frac{Z_0 \sqrt{\epsilon_{re}}}{c} \times \ell \quad (7)$$

However, the calculation of the capacitance of the interdigital capacitor is more complex than calculating resistance and inductance values. In order to calculate capacitance value of the interdigital capacitor, the Eq. (8), (9) and (10) can be used.

$$C = \frac{\epsilon_r \epsilon_0 10^{-3}}{18\pi} \frac{K(k)}{K'(k)} (N-1)\ell \quad (\text{pF}) \quad (8)$$

$$\frac{K(k)}{K'(k)} = \begin{cases} \frac{1}{\pi} \ln\left(\frac{2(1+\sqrt{k})}{1-\sqrt{k}}\right), & 0.707 \leq k \leq 1, \\ \frac{\pi}{\ln\left(\frac{2(1+\sqrt{k'})}{1-\sqrt{k'}}\right)}, & 0 \leq k \leq 0.707. \end{cases} \quad (9)$$

$$k = \tan^2\left(\frac{\pi a}{4b}\right), \quad a = \frac{W}{2}, \quad b = \frac{W+S}{2}, \quad k' = \sqrt{1-k^2}. \quad (10)$$

The phase difference provided by the interdigital capacitor can be determined by substituting the necessary values into the formula that gives the phase difference of the RLC circuit. Once the required phase shift for each antenna element is calculated based on the desired elevation and azimuth angles for beam steering, the interdigital capacitors can be designed to provide the necessary phase differences.

D. Phased Array Antennas

Overcoming propagation losses is especially helped by phased arrays. These antennas reduce, diminish and multipath effects by dynamically directing beams and concentrating energy in desired directions. Phased arrays improve impedance bandwidth in design, so improving matching over a broad frequency spectrum. Phased array designs are also perfect for integration into space-constrained platforms since they can achieve small sizes without sacrificing performance.

Starting with feeding type choice, design of the array antenna proceeds. Although there are several feeding techniques that can be chosen, our feeding type should be compatible with interdigital capacitors in the later design phases. Consequently, coaxial feeding is chosen to be used since IDCs can be implemented to the coaxial feeding to provide phase shift to the antenna elements.

Determining the combined radiation pattern of the array elements, the array factor (AF) is a fundamental component in phased array design. Array factor formula can be observed in the Eq. (11).

$$AF = \sum_{m=0}^{N-1} a_m e^{j(\alpha_m + \beta d \cos \theta)} \quad (11)$$

N denotes the total number of elements in the array in Eq. (11), hence directly affects the resolution and gain of the radiation pattern. The amplitude of every element denoted as a_m controls the relative contribution of the m -th element to the general radiation pattern. Beam steering by means of the constructive or destructive interference of the radiated waves depends critically on the phase shift applied to the m -th element, α_m . Furthermore term shown as “ $\beta d \cos \theta$ ” is phase shift brought about by element spacing.

The element factor times the array factor determines the overall radiation pattern of a phased array. Whereas the array factor accounts for the interaction among elements, the element factor shows the radiation properties of individual elements. Their combined define the general antenna system behavior. This is shown in Fig. 7 where the total radiation characteristics of an array antenna system is obtained by multiplying radiation characteristics of a single element by array factor.

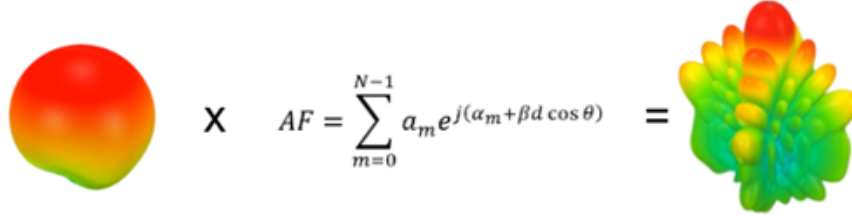


Figure 7: Visualization of the radiation pattern formation in a phased array antenna system

Both linear and planar arrays are extensively applied in phased array antenna systems for beamforming and beam steering. Depending on their arrangement, the phase shifting needs and the application, these arrays have different

properties. The antenna elements in a linear array line either horizontally or vertically. Phase shifts applied along the array axis produce beam steering in linear arrays. Equation (12) allows one to see the phase shift needed for every antenna element in a linear array.

$$\Delta\Phi = \frac{2\pi d \sin \theta}{\lambda} \quad (12)$$

In Eq. (12), “d” represents element spacing along the array axis, θ is angle of the beam from the array axis [12]. This formula shows that as the angle of the beam increases, the phase shift required to steer the beam also increases. This also can be visually observed in Fig. 8.

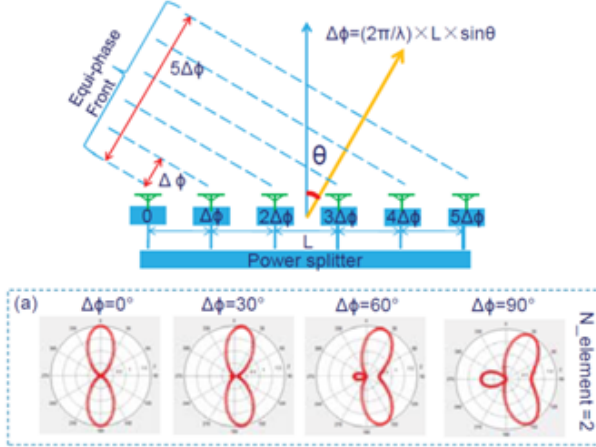


Figure 8: Beam steering in a linear phased array antenna by applying increasing phase shifts ($\Delta\phi$) to each element, shifting the main lobe in the radiation pattern [13]

Planar arrays, on the other hand, consist of antenna elements arranged in a two-dimensional grid, usually rectangular. Beam steering in planar arrays requires phase shifts in both the x- and y-axes. This two-dimensional phase shifting enables the beam to be steered in both elevation and azimuth angles. For planar arrays, the phase shifts for the x- and y-axes are given in Eq. (13) and (14).

$$\alpha_x = -k d_x \sin \theta \cos \phi \quad (13)$$

$$\alpha_y = -k d_y \sin \theta \sin \phi \quad (14)$$

Here θ is elevation angle and ϕ is azimuth angle of the beam. In order to find phase steps at each antenna element at position (m, n) Eq. (15) can be used.

$$\varphi_{mn} = m \alpha_x + n \alpha_y \quad (15)$$

For a 2x2 planar phased array antenna, for example, m and n span from 0 to 1. Appropriate phase shifts applied to every element allow the whole array to generate a beam pointing in the required direction [14]. Planar arrays can steer in both elevation and azimuth; linear arrays drive the beam along a single axis. This provides more freedom in many kinds of applications. While in planar arrays phase shifts are applied in both the x and y-directions for 2D control, in linear arrays phase shifting occurs along one axis. But whereas planar arrays are more complicated, linear arrays have a simpler one-dimensional element arrangement. This project has selected a planar array since planar arrays are preferred in applications needing wide-angle scanning and multi-dimensional steering.

E. Design of 2x2 Phased Array Antenna

Simulations are conducted in HFSS to observe the characteristics of the phased array antenna and compare the differences with single element antenna. In Fig. 9, single element, coax-fed patch antenna and its 2x2 array can be observed. The physical parameters of the patch antenna used in this work, including dimensions of the patch, substrate, and coaxial feed, are detailed in Table 1.

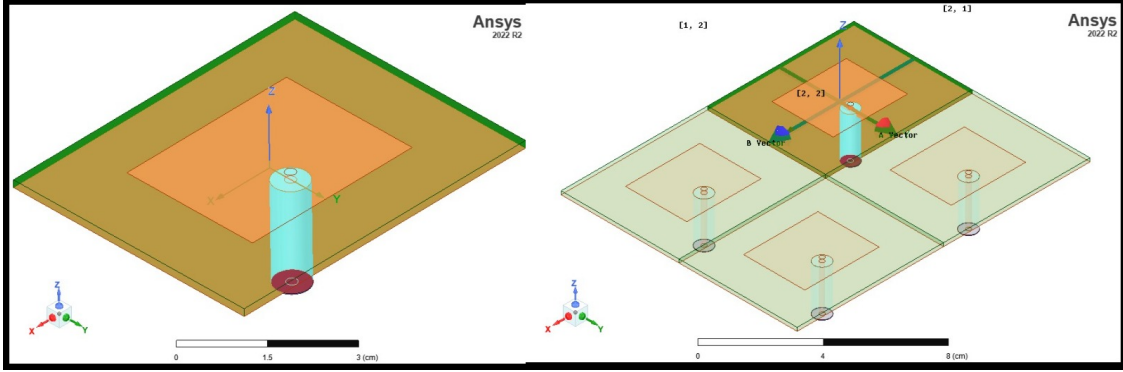


Figure 9: Single element antenna (left) and its corresponding array (right)

Parameter	Value	Unit	Parameter	Value	Unit
Antenna Dimensions			Feed Dimensions		
Patch width (X)	3.4	cm	Feed position X	0	cm
Patch length (Y)	2.8	cm	Feed position Y	0.49	cm
Substrate Dimensions			Inner conductor radius	0.104	cm
Substrate height	0.1575	cm	Outer conductor radius	0.354	cm
Substrate width (X)	6.7	cm	Feed length	2.08	cm
Substrate length (Y)	5.4	cm	Ground width (X)	6.7 (Substrate X)	cm
			Ground length (Y)	5.4 (Substrate Y)	cm

Table 1: Design parameters of the patch antenna modeled in Ansys HFSS [8].

Single element patch antenna is designed to operate at frequency of 2.4 GHz. Similarly, at phased array antenna, frequency of operation is 2.4 GHz simply because all elements are excited with correct amplitude. Also, element spacing is another important factor for operating at the same frequency. For optimal performance, the spacing should generally be less than or equal to half the wavelength, which is satisfied in our design.

If radiation patterns of two designs are compared, significant changes can be observed. First change is side lobes are introduced in phased array antenna. This allows enhancing maximum gain and directivity; however, it reduced the beamwidth, decreasing the coverage of the antenna. Radiation patterns of two designs can be observed in the Fig. 10.

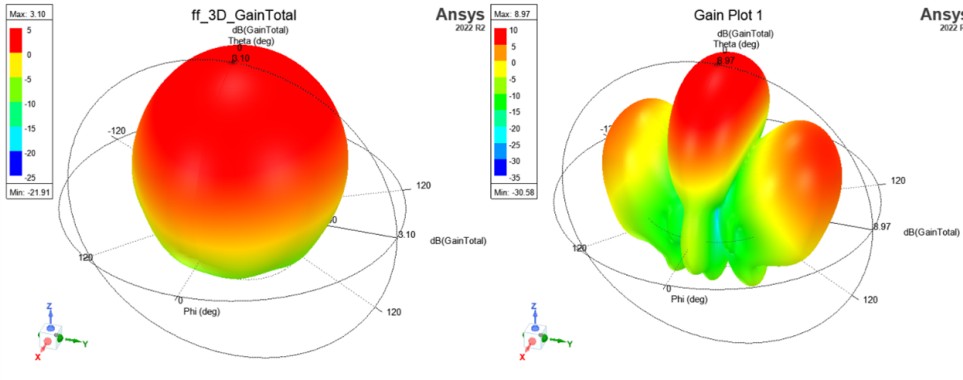


Figure 10: Comparison of radiation patterns of single element (left) and array antennas (right)

As it can be observed in Fig. 10., maximum gain is 3.1 dB in single element patch antenna and 8.97 dB in array antenna. This implies significant maximum gain and directivity increase in the array antenna. Beamwidth is defined as the angular range where the gain drops by 3 dB from the maximum gain in the main lobe. This is known as the

half-power beamwidth (HPBW). In order to observe beamwidth decrease in the phased array antenna, 3 dB drop points should be observed. In Fig. 11 beamwidths of the both single patch antenna and phased array antenna can be observed.

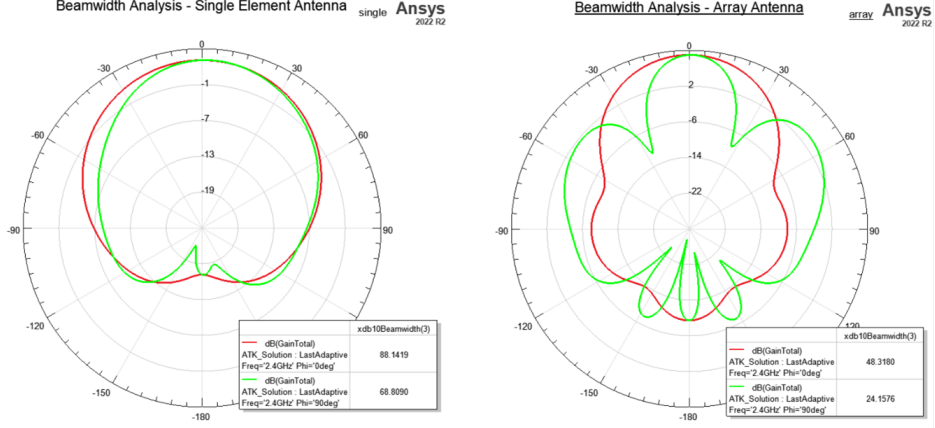


Figure 11: 2D radiation patterns to show beamwidth comparison of single and array antennas.

As it can be observed from Fig. 11, beamwidth of the phased array antenna is approximately 40° less at $\phi = 0$ and 42° less at $\phi = 90$ than single element patch antenna. This tradeoff has to be made in order to increase beam steering capabilities and maximum gain. In phased array antennas, the theta (θ) angle represents the elevation of the antenna's beam, defined as the angle from the positive z-axis to the vector, ranging from 0° (upward) to 180° (downward). The phi (ϕ) angle represents the azimuth of the beam, describing the angle in the xy-plane from the positive x-axis, ranging from 0° to 360° . By adjusting the phase shifts applied to the antenna array elements, both θ and ϕ can be manipulated to steer the antenna's beam in any desired direction. Visual representation of those angles can be observed in Fig. 12a.

Larger arrays generally have narrower beamwidths and can achieve finer steering resolution. Since, in this project a 2x2 antenna array is used, lower beam steering capabilities is expected. In order to demonstrate beam steering capabilities of the phased array antenna, we can make a simplification and observe only azimuth angle and not elevation angle. Thus, ϕ angle is kept constant at $\phi = 0$. Maximum steerable angle can be observed with the help of grating lobes. These are unwanted secondary lobes that can appear as steered further. They become significant when their amplitude is close to the main beam's amplitude. Maximum steerable angle analysis of the phased array antenna can be observed in Fig. 12b.

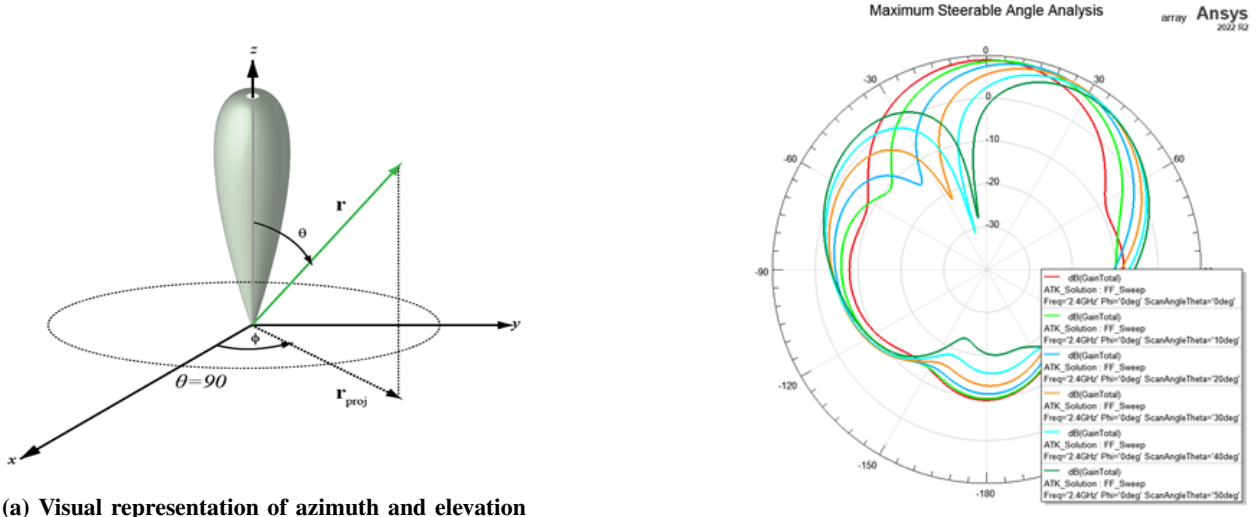


Figure 12: Azimuth/elevation definition (left) and corresponding radiation patterns (right).

As observed in Fig. 12b, as θ increased from 0 to 50° , side lobes become significant. At $\theta = 50^\circ$, sidelobe's maximum gain is almost the same with the main lobe, and that is an obstacle to scanning abilities. Since at $\theta = 45^\circ$, main lobe is still significant, it can be observed that, maximum steerable angle is approximately $\theta = 45^\circ$. In order to increase steering abilities, number of antennas in the array can be increased.

F. Calculation of Phase Shifts using MATLAB

MATLAB allows to compute phase shifts for the matching angles in a phased array system. These computations aim to guarantee that, depending on the given elevation and azimuth angles, every antenna element gets the suitable phase shift to guide the beam in the desired direction. MATLAB codes are found in the part on "Appendices".

The MATLAB code given uses several inputs to determine the required phase shifts. These inputs comprise the "scan frequency," (in our project 2.4 GHz), the "elevation angle," (θ), the "azimuth angle," and the "base phase," set to zero. The phase shifts for the related angles that define the direction of the antenna beam are calculated using these principles. Using elevation and azimuth angles, the code determines the phase shifts for every antenna element in the array. The phase shift equations consider the direction the beam must be guided as well as the geometry of the array. The array can steer the beam exactly to the needed direction by varying the phase for every antenna element. The HFSS simulations also confirm computed phase shift values given by MATLAB. These computations help the antenna system to be built to produce phase shifts found in the MATLAB code given in Listing 1 at the "Appendices" part. Interdigital capacitors can thus be built to produce these phase shifts.

The phase values computed in MATLAB are shown in Fig. 13 and applied to the corresponding antenna elements in the simulation. For every port, the phase changes are shown together with computed values for the matching array elements. These are the values ascertained using MATLAB; the values for the phases are displayed in radians. The phased array antenna system is thus able to provide exact beam steering since the code guarantees that the antenna elements are fed with the proper phase values to guide the beam to the desired direction.

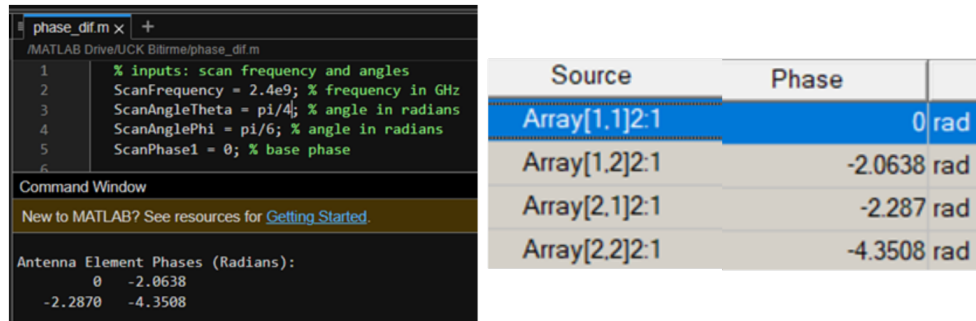


Figure 13: Phase values are calculated in MATLAB and those calculated phases are applied to the antenna elements.

With the computed phase values applied, the 3D radiation pattern of the antenna is displayed Fig. 14. The simulation results in HFSS show how the radiation pattern of the antenna changes in response to the applied phases, so enabling the beam to be steered in particular directions. The pattern shows the intended main lobe and side lobes, so illustrating how the beam might be steered using the given phase shifts. A 3D graph shows the gain distribution, so highlighting the antenna's general performance and steering capacity.

By using a comparison of the radiation patterns for different elevation and azimuth angles, the next set of figures verifies the effectiveness of the applied phase shifts. The radiation patterns for phi equal 30 degrees and theta equal 45 degrees are shown in Fig. 15. Whereas the plot on the left shows the 2D radiation pattern for a 45-degree elevation angle (theta), the plot on the right shows the pattern for a 30-degree azimuth angle (phi). These radiation patterns confirm the phase shifts imposed on the antenna elements, so ensuring that the specified phase values efficiently guide the beam to the desired angles.

The accuracy of the phase shifts applied to the antenna array elements confirmed by the HFSS simulations guarantees the intended beam steering. The validation process guarantees accuracy of the MATLAB implementation and alignment of the simulation results with the expected ones. Phase shifts applied successfully to the antenna elements

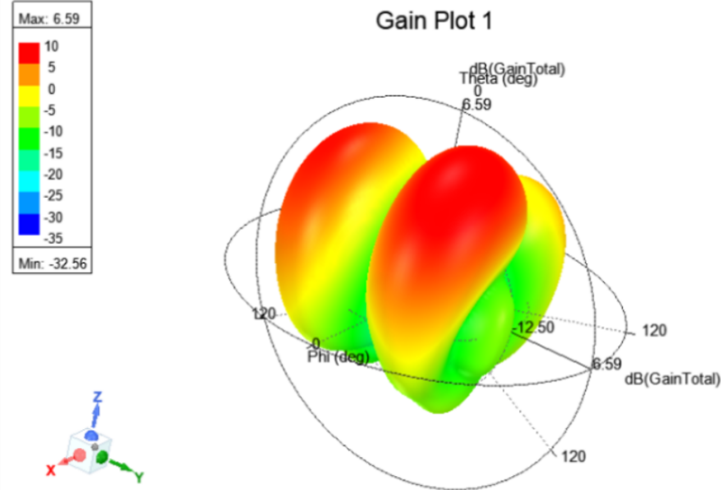


Figure 14: 3D radiation pattern of the antenna with calculated phases.

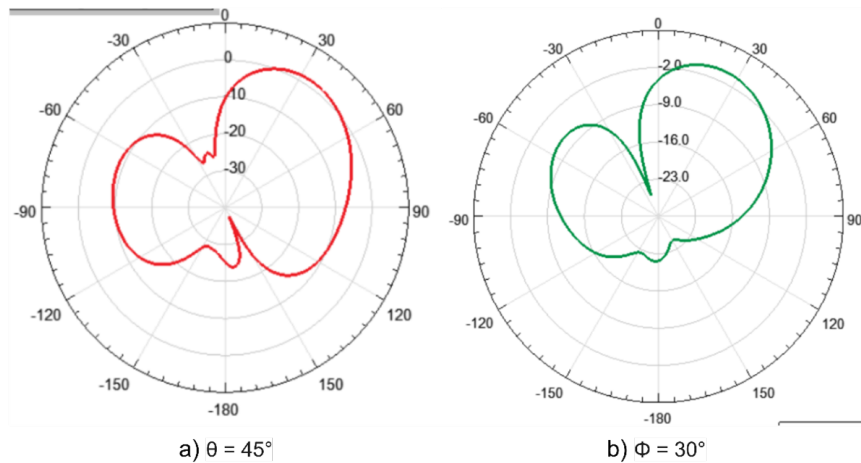


Figure 15: HFSS results validating provided phases to antenna elements supply desired direction.

confirm the viability and efficiency of the phased array antenna design, so fitting for practical uses requiring dynamic beam steering and exact control over radiation patterns.

G. Interdigital Capacitor Design with MATLAB

In order to provide a phase shift to one of the antenna elements, IDC is used. IDC is acting like an RLC circuit thus it provides a phase shift to the transmission line. Main challenges in the IDC design are fabrication friendliness, designing at a specific operating frequency, and providing the necessary phase shift. Thus we have to parametrize the IDC elements such as the number of fingers used in the IDC and finger length. For this reason, RF PCB Toolbox of MATLAB is used to design IDC for our project. For ease of fabrication, FR4 is chosen as the substrate of our IDC with provided properties in Table 2. Edge finger gap and finger width parameters are kept constant at 0.5 mm due to fabrication constraints.

In order to optimize IDC, finger length and number of fingers are optimized. Design is initially started at 20 mm of finger length and 4 number of fingers. This provides a 2.35 GHz operating frequency. This has to be optimized for actual operating frequency of 2.4 GHz. All optimized IDC parameters are provided in Table 3.

An interdigital capacitor (IDC) can be modelled at resonance by its total capacitance C_{tot} and parasitic inductance

Property	Value
Name	FR4
Substrate Permittivity (ϵ_r)	4.4
Substrate Loss Tangent ($\tan \delta$)	0.02
Thickness of the substrate	1.6mm
Conductor thickness (copper)	5 μm

Table 2: Substrate and conductor properties used in the IDC design.

Parameter	Variable	Value	Description
Finger length	L	19.80 mm	Finger length
Number of fingers	N	4	Total number of fingers
Finger width	w	0.5 mm	Width of each finger
Finger spacing	s	0.3 mm	Spacing between adjacent fingers
Edge gap	g	0.5 mm	Gap at the ends of the fingers
Port line width	W_p	3.0 mm	Width of the input/output port line
Ground plane width	W_g	10 mm	Width of the ground plane
Design frequency	f_0	2.4 GHz	Target resonance frequency

Table 3: Intital interdigital capacitor (IDC) geometry and sweep parameters.

L_p as shown in the Eq. (16) where L_p is the parasitic inductance and C_{tot} the total capacitance.

$$f_0 = \frac{1}{2\pi\sqrt{L_p C_{\text{tot}}}} \quad (16)$$

The total capacitance is approximated as shown in the Eq. (17), according to the Eq. (8), (9) and (10).

$$C_{\text{tot}} \approx (N - 1)C_{\text{finger}}, \quad C_{\text{finger}} \approx \frac{\epsilon_0 \epsilon_{\text{eff}} L}{\pi} \ln \left[\csc \left(\frac{\pi g}{2(w+g)} \right) \right] \quad (17)$$

Hence, relation between operating frequency and IDC sweep parameters can be observed as shown in the Eq. (18).

$$f_0 \propto \frac{1}{\sqrt{(N - 1)L}} \quad (18)$$

To shift resonance from $f_{0,\text{old}}$ to $f_{0,\text{new}}$, adjusting L and N iteratively is needed. This can be achieved as shown in the Eq. (19) and (20).

$$L_{\text{new}} = L_{\text{old}} \left(\frac{f_{0,\text{old}}}{f_{0,\text{new}}} \right)^2 \quad (19)$$

$$N_{\text{new}} - 1 = (N_{\text{old}} - 1) \left(\frac{f_{0,\text{old}}}{f_{0,\text{new}}} \right)^2 \quad (20)$$

After the iterative process, 4 total fingers and 19.80 mm finger length is found to be the optimum sweep parameters. After the optimized parameters, scattering parameters of the IDC can be observed as seen in Fig. 16a and resulting IDC can be observed in Fig. 16b. Another important parameter of the IDC is its characteristic impedance. It should be selected as 50Ω in order to minimize impedance mismatch. In the simulations, characteristic impedance of the IDC is calculated as 50.88Ω which is enough to minimize signal losses due to mismatch. Optimization code is provided in the Listing 3 at "Appendices" section.

We insert a small phase-shifting element, IDC, into our antenna feed network. The IDC precisely controls the radiation phase of the antenna by changing its geometry, so adding a frequency-dependent electrical delay between the feed line and the antenna, without resorting to long transmission-line stubs. From the two-port insertion parameter S_{21} of the simulated network, the phase shift introduced by the IDC (together with its feed structure) is obtained. Denoting the frequency as f the insertion phase $\phi(f)$ is just the argument of $S_{21}(f)$. The Eq. (21) shows this.

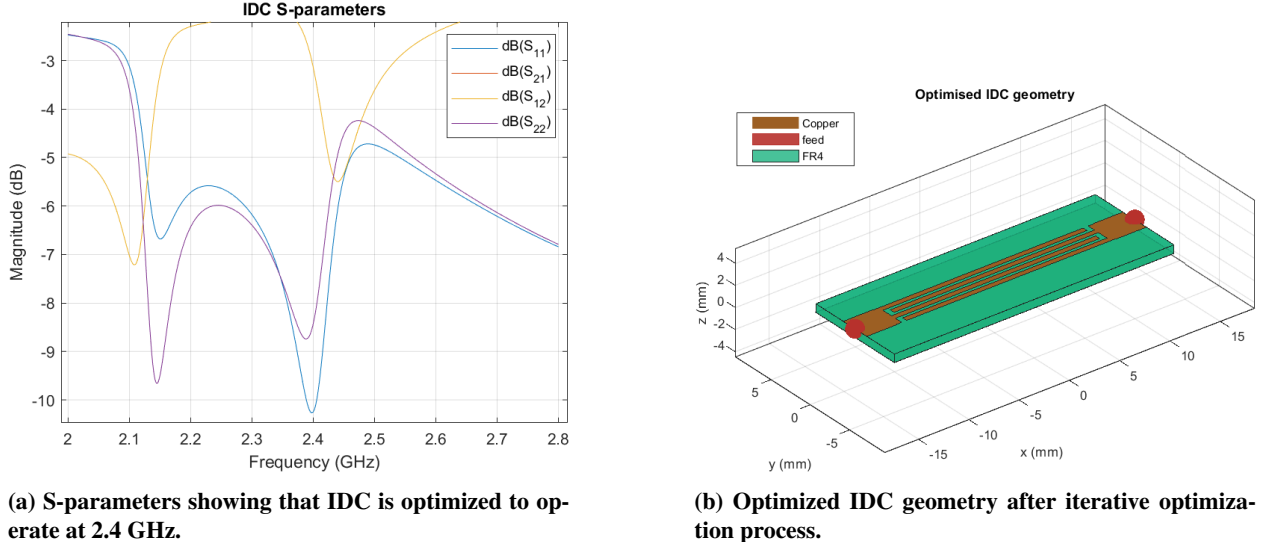


Figure 16: Optimized IDC with its S-paramter values.

$$\phi(f) = \angle S_{21}(f) = \arg\{S_{21}(f)\} \quad (21)$$

In Eq. (21), $\arg\{\cdot\}$ yields the complex phase in radians. For our optimized design with specified dimensions in Table 3, with $L = 19.80$ mm, the simulated insertion phase at the design frequency $f_0 = 2.40$ GHz is $\phi(f_0 = 2.40) = 29.8^\circ$. Thus, the IDC contributes a phase lag of approximately 0.52 radian at 2.4 GHz, which is the quantity used when integrating this element into the antenna feed network. Other specifications of the IDC is provided in Table 4.

Property	Value
Capacitance (C)	1.71 pF
Characteristic impedance (Z_0)	50.88 Ω
Insertion phase (ϕ)	0.52 rad
Return loss (S_{11})	-10.24 dB

Table 4: Properties of IDC at resonant frequency of 2.40 GHz.

H. Fabrication

IDC and patch antenna elements are fabricated using a CNC3018 Pro PCB engraver. The PCB engraving process is illustrated in Figure 17. The fabricated patch antenna and interdigital capacitor are shown in Figure 18.

There were four stages to the building process. Paint covered both sides of the double-sided copper-clad FR4 board completely. Using a PCB engraver, areas meant to remain as substrate were etched. The copper from the areas where the paint had been removed was etched away using a mixture of hydrogen peroxide (H_2O_2) and hydrochloric acid (HCl). This guaranteed that while the ground plane stayed on the bottom, the patch stayed on the top side. At last thinner helped the paint to be taken off.

Based on the necessary conductor dimensions, a suitable coaxial cable was chosen to link the built antenna to the measuring equipment. The design demanded an outer conductor radius of 0.354 cm and an inner conductor radius of 0.104 cm. Standard coaxial cables were compared to find that RG58 is more suitable than RG174. RG58 is closer to the needed values than RG174 even if neither cable completely satisfies the design criteria since RG58 boasts a larger inner conductor radius (about 0.05 cm) and an outer conductor radius (about 0.15 cm). For this design, RG58 was thus selected.

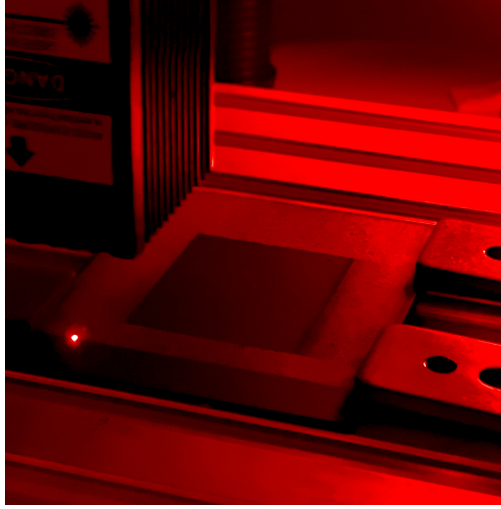
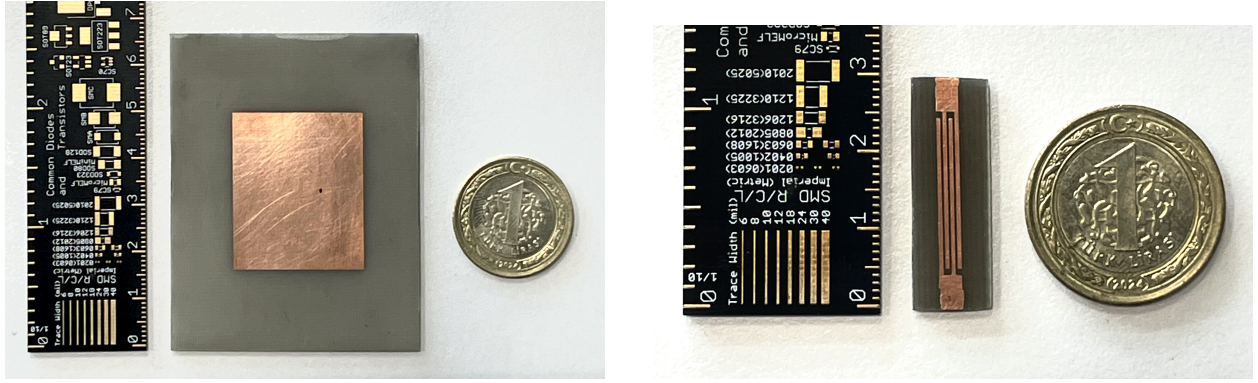


Figure 17: PCB engraving process using CNC3018 Pro.



(a) Fabricated patch antenna

(b) Fabricated interdigital capacitor

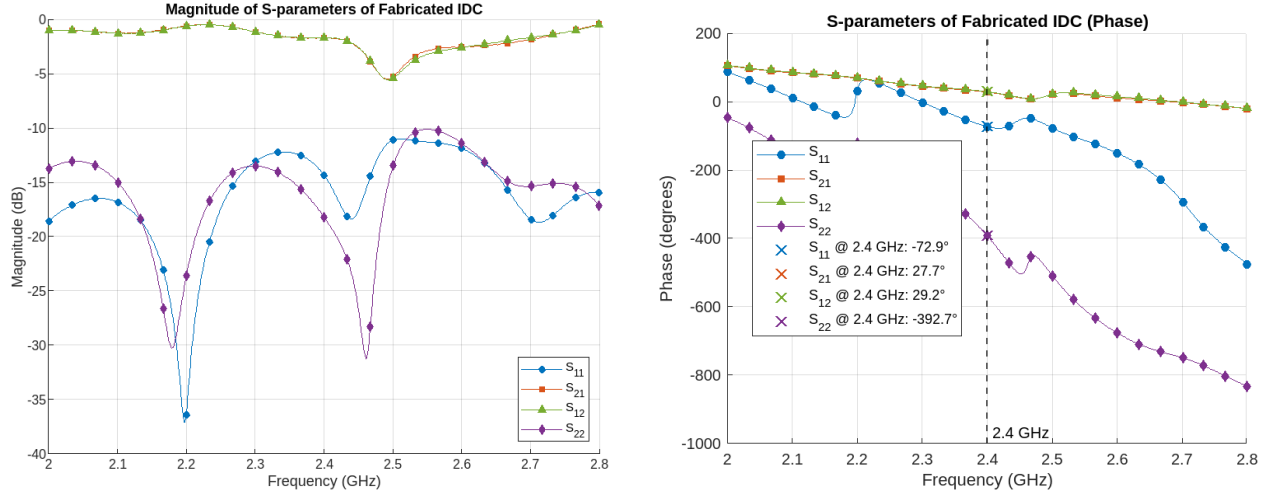
Figure 18: Fabricated RF structures.

I. Fabrication Measurements

The fabricated interdigital capacitor (IDC) was characterized using a vector network analyzer (VNA). Figure 19a shows the measured magnitude of the S-parameters. The deep resonance near 2.2 GHz (approximately -37 dB) and the secondary dip near 2.5 GHz indicate slight frequency shifts relative to the design target. At 2.4 GHz (marked), the return loss $|S_{11}|$ is about -15 dB. Also, Figure 19b shows the measured phase. At 2.4 GHz, the insertion phase $\angle S_{21}$ is approximately 27.7° , which is within 2.1° of the simulated value. The reflection phases at 2.4 GHz are $\angle S_{11} = -72.9^\circ$ and $\angle S_{22} = -392.7^\circ$.

Figure 20a shows input and output impedances of fabricated IDC. At 2.4 GHz (vertical dashed line), $|Z_{in}| = 55.8 \Omega$ and $|Z_{out}| = 61.5 \Omega$. In simulation, both ports were matched to 50Ω at 2.4 GHz; the measured offsets of $+4.9 \Omega$ (input) and $+10.6 \Omega$ (output) arise from etching tolerances and FR4 dielectric-constant variation. Additionally, Figure 20b present the capacitance of IDC. The marker at 2.4 GHz indicates $C = 1.672 \text{ pF}$. In simulation, the IDC capacitance at resonance was 1.71 pF , so the measured value differs by -2.3% . The negative and spiking values outside the main band reflect reactive measurement uncertainty far from resonance.

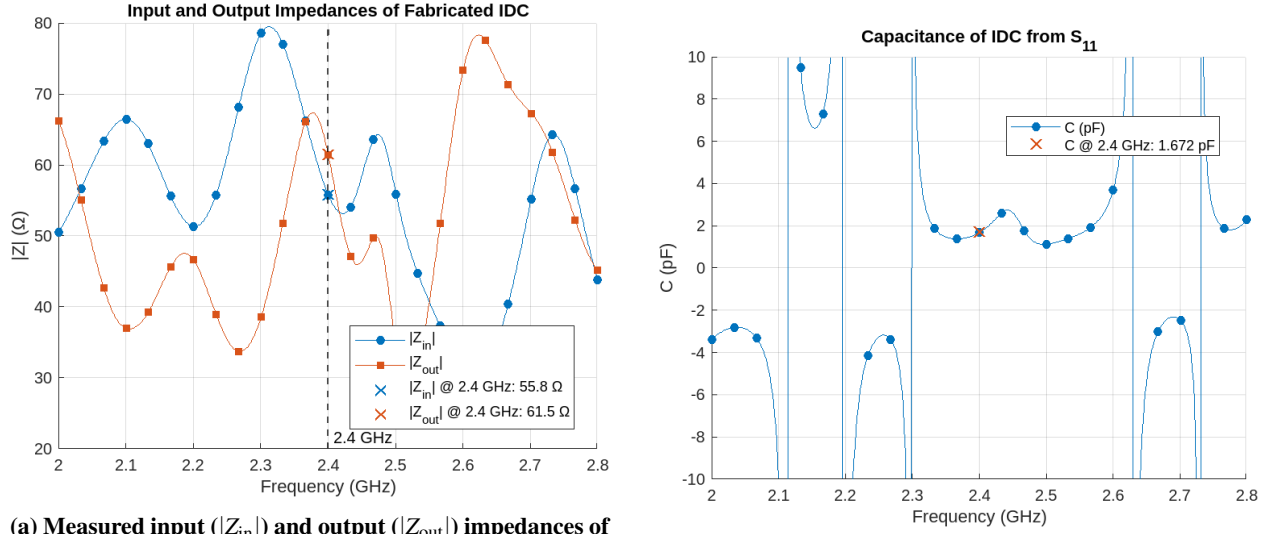
In simulation, the IDC was designed to resonate exactly at 2.40 GHz with a return loss of approximately -10.2 dB. Instead, the fabricated device exhibits its deepest reflection minimum near 2.20 GHz (-37 dB) and a secondary null near 2.50 GHz. Although the primary resonance shifted downward by about 200 MHz, at 2.40 GHz the measured return loss is still -15 dB, indicating acceptable matching at the design frequency. This shift is likely caused by



(a) Measured magnitude of the S-parameters of the fabricated IDC.

(b) Measured phase of the S-parameters of the fabricated IDC.

Figure 19: (a) Measured magnitude of the S-parameters of the fabricated IDC. (b) Measured phase of the S-parameters of the fabricated IDC.



(a) Measured input ($|Z_{in}|$) and output ($|Z_{out}|$) impedances of the fabricated IDC.

(b) Capacitance of the fabricated IDC inferred from S_{11} .

± 0.1 mm etching tolerances in finger width and spacing and by the actual FR4 dielectric constant being slightly different from the nominal value.

At 2.40 GHz, the insertion phase $\angle S_{21}$ from measurement is 27.7° , compared to the simulated 29.8° . The -2.1° deviation corresponds to the fabricated IDC still delivers the intended 0.52 rad phase shift.

Figure 20a shows that the input impedance at 2.40 GHz is 55.8Ω and the output impedance is 61.5Ω . In simulation, both ports were matched to 50.9Ω at that frequency; the measured offsets of $+4.9 \Omega$ and $+10.6 \Omega$ are caused by extra PCB trace lengths and slight misalignment of the capacitor fingers. Despite these offsets, both impedances remain within $\pm 20\%$ of the nominal value, which is acceptable for a passive phase-shifter element in a phased-array feed network.

The capacitance extracted from S_{11} (Figure 20b) is $C_{meas} = 1.672 \text{ pF}$ at 2.40 GHz. Simulation predicted $C_{sim} = 1.71 \text{ pF}$ (Table 4), so the measured capacitance is about -2.3% lower. This discrepancy likely arises from slight

over-etching of the finger gaps (nominally 0.3 mm) and the FR4 permittivity being marginally higher than assumed. However, the measured value remains well within standard FR4 manufacturing tolerances.

Overall, the measured data demonstrate that the fabricated IDC closely tracks the simulated performance, with only minor frequency shifts and impedance offsets. The insertion phase at 2.40 GHz (27.7° measured vs. 29.8° simulated) confirms that this passive element will produce the desired 0.52 rad phase lag in the feed network. Although the resonant dip in $|S_{11}|$ shifted by approximately -200 MHz, the IDC still maintains a return loss better than -15 dB at the design frequency. The capacitance and port impedances lie within $\pm 10\%$ of their simulated values, indicating successful fabrication. These results validate the IDC as a compact, reliable phase-shifting element for the 2×2 phased-array antenna feed.

Figure 21 shows the measured reflection coefficient (S_{11}) versus frequency for the four fabricated antennas. Each curve exhibits a clear resonance dip in the vicinity of the 2.4 GHz ISM band, demonstrating that the antennas operate close to the design target of 2.4 GHz.

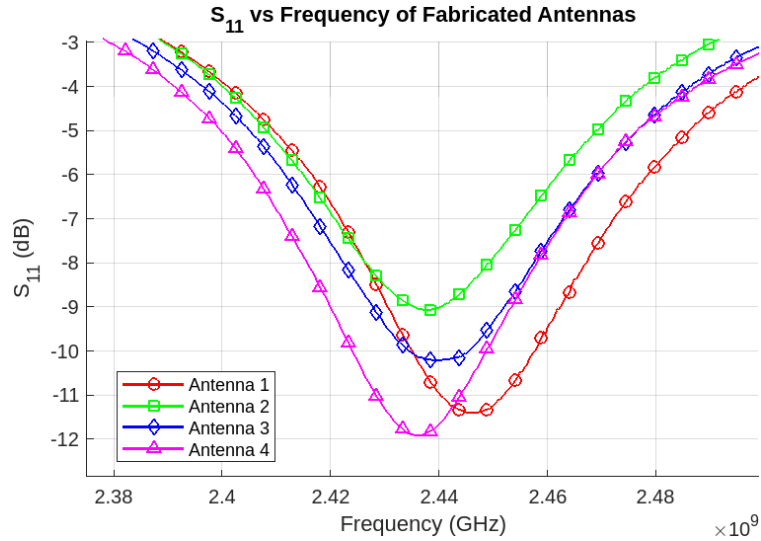


Figure 21: S_{11} versus frequency for Antennas 1–4. Resonance dips are observed near 2.44 GHz (Antenna 1), 2.43 GHz (Antenna 2), 2.445 GHz (Antenna 3), and 2.44 GHz (Antenna 4), all within ± 50 MHz of the 2.4 GHz design frequency.

As seen in Fig. 21, all four prototypes achieve minimum dip within the frequency range 2.38–2.48 GHz, confirming good impedance matching and successful fabrication. The slight variations in resonant frequency (± 5 – 10 MHz) arise from manufacturing tolerances and material inhomogeneities but remain well within the acceptable bandwidth for the 2.4 GHz ISM application.

J. Experimental Setup and Signal Testing with SDR

Two separate experimental configurations were built and compared in order to assess how phase shifting affected the beam steering capability of the intended phased array antenna. Both times a 2×2 patch antenna array was employed, but in one configuration an interdigital capacitor (IDC) was placed into the feed line of one antenna element to provide a deliberate phase shift.

The IDC introduces a frequency-dependent delay into the transmission line, so acting as a passive phase shifter. This produces a modified phase excitation for the particular antenna element, so changing the total radiation direction of the array.

Figure 22 presents the typical phased array antenna configuration devoid of IDC. By means of equal-length cables and standard splitters, all four elements are directly connected and produce consistent phase excitation over the array.

In contrast, Figure 23 shows the modified setup in which an interdigital capacitor is added to the feed line of one element. This introduces a phase delay specific to that element, resulting in asymmetric excitation and beam steering.

The efficiency of passive phase shifters such as IDCs is demonstrated in this experiment for real-time beam steering in small phased arrays. Just adding phase offsets allows one to control the beam without using active components or

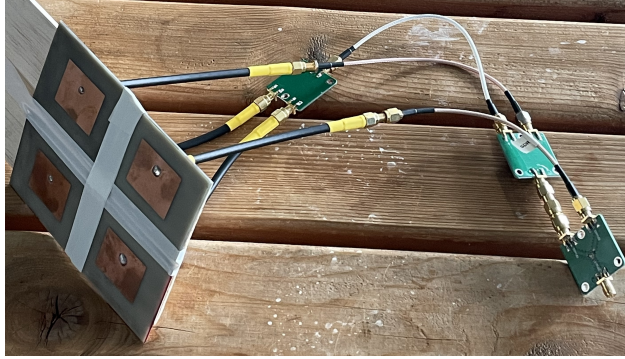


Figure 22: Antenna setup without IDC: All four elements are fed uniformly, resulting in symmetric radiation centered in the forward direction.

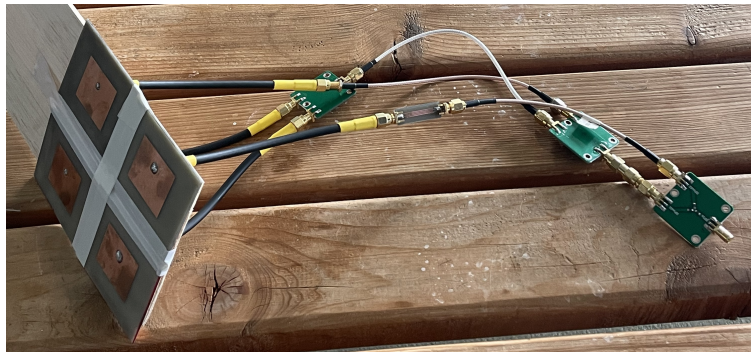


Figure 23: Antenna setup with IDC: An interdigital capacitor is inserted into one of the feed lines, introducing a phase shift that alters the direction of the radiation pattern.

sophisticated circuitry.

The built-in phased array antenna and interdigital capacitor performance was evaluated by means of a real-time signal transmission and reception test. The experimental setup included two software-defined radios (SDRs). Having a commercial dipole antenna, the second HackRF was the receiver; one HackRF ran as the transmitter while linked to the built-in phased array antenna.

Transmission was carried out using the 2.4 GHz ISM band; this matches the design frequency of the patch antenna array and the IDC resonance point. The test sought to verify that the built antenna could effectively broadcast signals at the assigned frequency and that a standard receiving antenna could regularly capture the radiated signals.

The signal testing devices are shown in Figure 24. The left gadget in the picture is the HackRF linked to the built-in antenna for signal broadcast. The HackRF with a dipole antenna set for signal reception is the correct tool.

To accurately observe the radiation characteristics of the fabricated phased array antenna, a far-field measurement setup was implemented at the ITU Aerospace Research Center. The goal of this experiment was to ensure that the receiving dipole antenna was positioned in the far-field region of the transmitting antenna, where the angular distribution of the radiated field becomes independent of the distance. Usually, the far-field distance (R_{ff}) is computed with the help Eq. (22).

$$R_{ff} \geq \frac{2D^2}{\lambda} \quad (22)$$

In Eq. (22), λ is the wavelength matching the operational frequency and D is the biggest dimension of the antenna aperture. On practical planar antenna arrays, a more conservative guideline of thumb is to guarantee that the receiving antenna is located at least 10λ away. For the operating frequency of 2.4 GHz, the wavelength is calculated as shown in the Eq. (23).

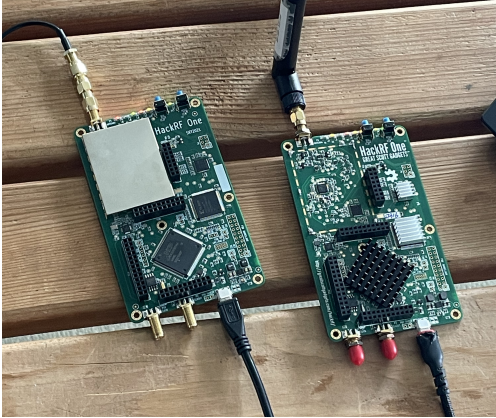


Figure 24: Signal transmission and reception setup using two HackRF One devices. The left unit transmits signals through the fabricated phased array antenna; the right unit receives signals using a dipole antenna.

$$\lambda = \frac{c}{f} = \frac{3 \times 10^8 \text{ m/s}}{2.4 \times 10^9 \text{ Hz}} = 0.125 \text{ m} \quad (23)$$

According to Eq.(23), the far-field distance can be calculated as shown in the Eq. (24).

$$R_{ff} \geq 10\lambda = 10 \times 0.125 \text{ m} = 1.25 \text{ m} \quad (24)$$

This led to exactly 1.25 m apart placement of the transmitting and receiving antennas to meet the far-field condition. The whole far-field measuring configuration is shown in Figure 25. The constructed 2x2 patch array antenna was coupled to a HackRF One SDR transmitter; the receiving end comprised a dipole antenna coupled to a second HackRF One and a laptop. GNU Radio Companion let one see the obtained signal on a waterfall diagram. The antennas were kept precisely apart using a measuring tape.



Figure 25: Far-field experiment setup at ITU Aerospace Research Center.

The MATLAB code provided in the section on Appendices indicates that, when a phase shift of roughly 0.52 radians (or 30 degrees) is applied to a single element in the 2x2 antenna array, the resultant beam direction is steered away from the broadside. The computation of the array factor reveals that in an elevation angle the main beam points $\theta = 33.5^\circ$. Therefore, in our physical testing using the interdigital capacitor to provide the required phase shift, we anticipate to find the peak signal intensity with regard to the broadside direction at almost 33.5° .

The beam steering capability of the 2x2 phased array antenna was experimentally confirmed by a set of tests at the ITU Aerospace Research Center. Every test used the array antenna as the transmitter; the observation point was

a dipole antenna coupled to a HackRF receiver. The antennas were positioned 1.25 meters apart in order to ensure far-field conditions as calculated before.

Two configurations were investigated: with and without the feed network of one antenna element including an interdigital capacitor (IDC). The IDC shows a phase change meant to direct the beam. The test method consisted in rotating the antenna configuration to four discrete angles relative to the broadside direction: 0° , 30° , 60° , and 90° . Using a waterfall diagram to track signal strength and find the direction of the maximum beam, the obtained signal was observed for every rotation. Figure 26 shows the setup during the angular sweep at all four test orientations.

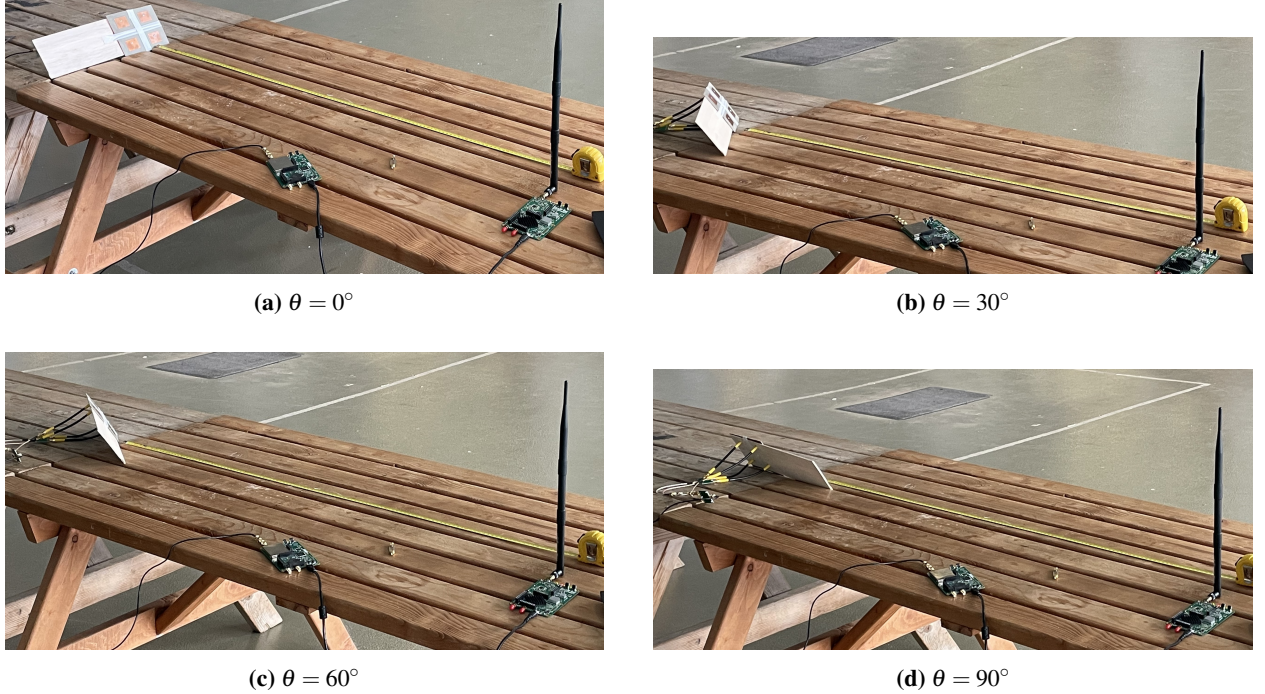


Figure 26: Test setup views for four different angles $\theta = 0^\circ, 30^\circ, 60^\circ$, and 90° . The received power is visualized using a waterfall diagram to observe beam alignment at each orientation.

Eight measurements in all, four with the IDC and four without were taken. MATLAB analysis in the Appendices indicates that the expected applied phase shift of 0.52 radians should steer the beam towards $\theta = 33.5^\circ$. Consequently, the strongest signal reception during the IDC-included test should arise when the receiver is oriented almost 30° off-axis. Peak signal observations in the relevant waterfall diagram confirmed this prediction: passive phase control with an IDC effectively results in beam steering.

For two test cases—with and without the IDC the signal strength visualization (waterfall plots) acquired by the HackRF receiver at four different angles ($\theta = 0^\circ, 30^\circ, 60^\circ, 90^\circ$) is presented here.

Results for the IDC included configuration are shown in Figure 27. Confirming the expected beam steering effect from the applied 0.52 radians phase shift, the peak signal strength (shown by the brilliant yellow vertical band) is seen at $\theta = 30^\circ$.

Figure 28 presents the same angular measurements without the IDC. As expected, the maximum reception occurs at $\theta = 0^\circ$, which aligns with the broadside direction when all elements are excited with equal phase.

V. Results and Conclusion

This work aimed to design, fabricate, and experimentally validate a 2x2 phased array antenna system to be able to electronic beam steering at 2.4 GHz for aviation communication uses. To guarantee a complete and functional implementation over the project, theoretical grounding, electromagnetic simulation, hardware prototyping, and measurement-based validation was used in this regard. With a practical, low-cost substitute for active beamforming

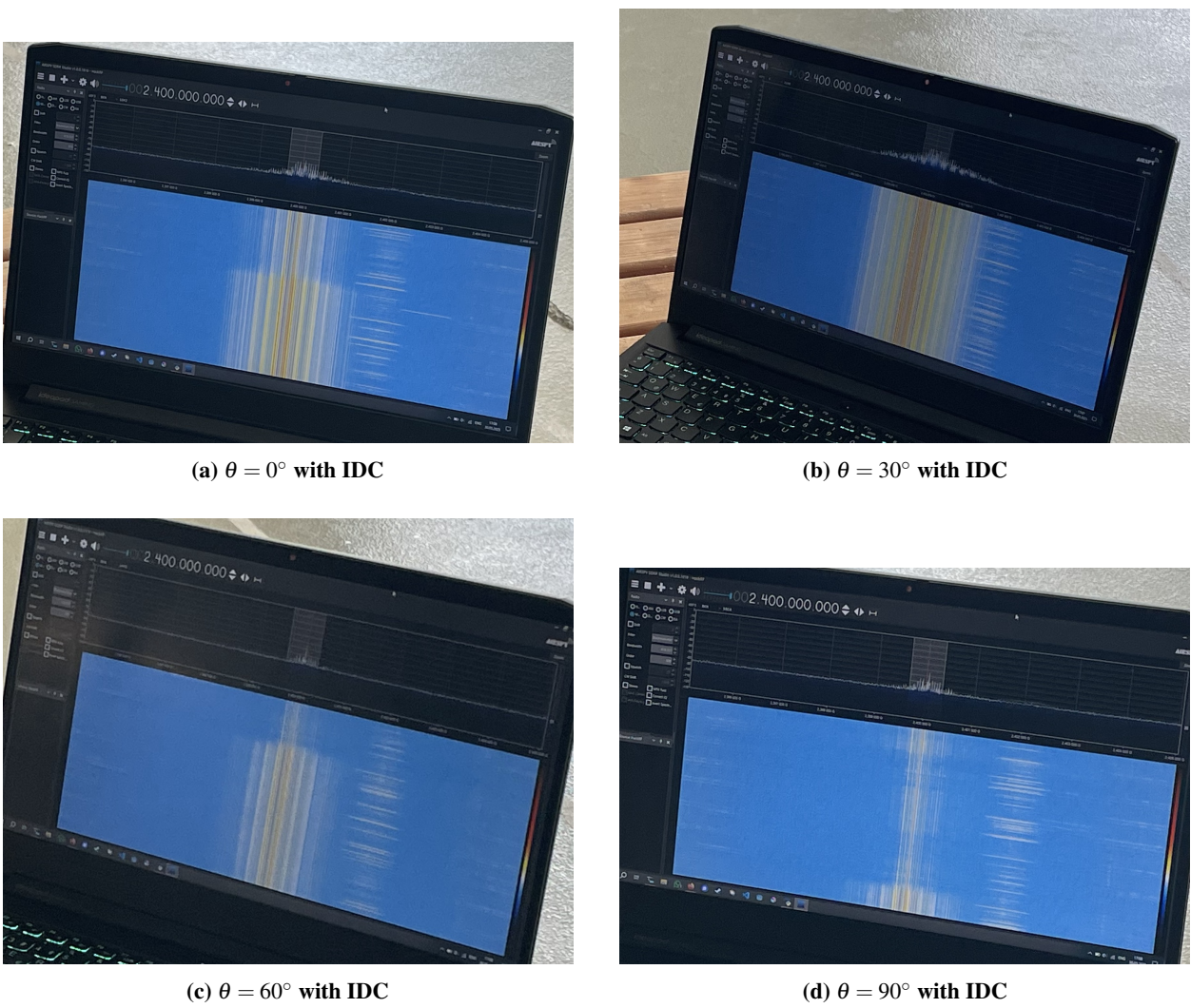
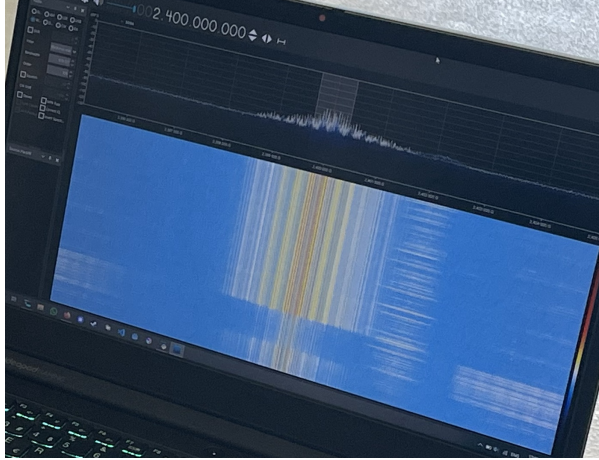


Figure 27: Waterfall diagrams with IDC inserted. Maximum signal intensity is observed at $\theta = 30^\circ$, indicating successful beam steering due to the applied phase shift.

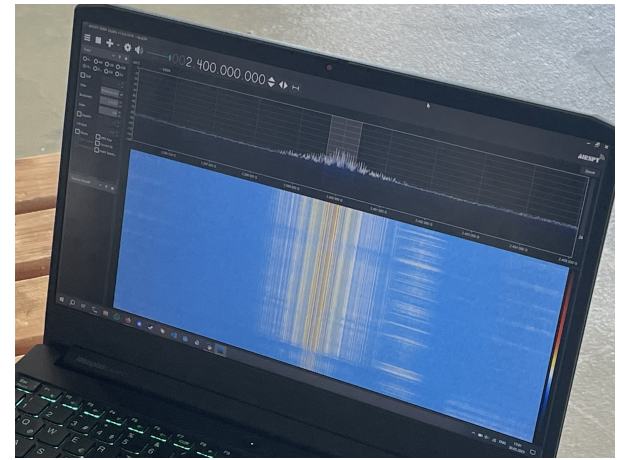
systems, microstrip patch antennas and interdigital capacitors (IDCs) were especially underlined as passive phase-shifting elements.

Microstrip patch antennas, a widely used structure in aerospace and wireless systems owing to their low profile, planar configuration, and simplicity of fabrication built the foundation of the phased array system. These antennas were examined closely with regard to their dimensions, effective dielectric constant, bandwidth, and fringing field effects. Patch width and length equations were derived using analytical models; these were validated by HFSS simulations. Designed for resonance at 2.4 GHz, the array comprised four edge-fed patch antennas arranged in a 2×2 configuration. The array reached a peak gain of 8.97 dB, much higher than the 3.1 dB found in a single-element design according to simulation results. In the $\phi = 0^\circ$ plane and 42° plane, the half-power beamwidth (HPBW) was lowered by roughly 40° showing enhanced directivity and spatial resolution. Beyond which grating lobes started to compromise main beam clarity, the array also displayed a maximum effective steering angle of $\theta \approx 45^\circ$.

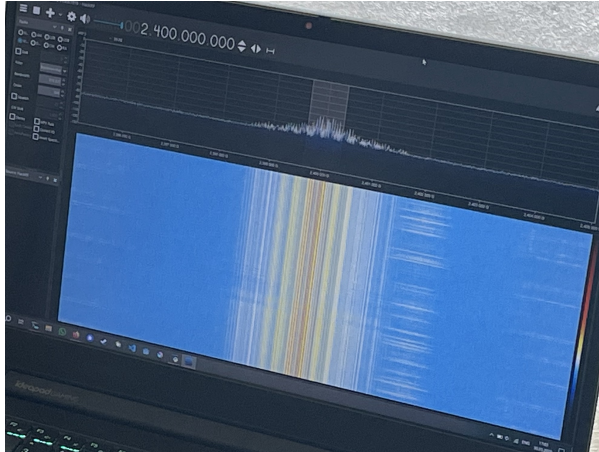
In the project we examined the mathematical formulation of beamforming using both the array factor and element factor, derivation of phase shift principles, and theoretical modeling of patch antennas. Based on elevation (θ and azimuth ϕ angles) MATLAB computed the necessary phase shifts for any intended beam direction. MATLAB scripts based on beam steering logic included array geometry, inter-element spacing, and frequency as inputs. Complete-wave HFSS simulations validated these computations. MATLAB, for instance, predicted beam redirection to $\theta = 33.5^\circ$



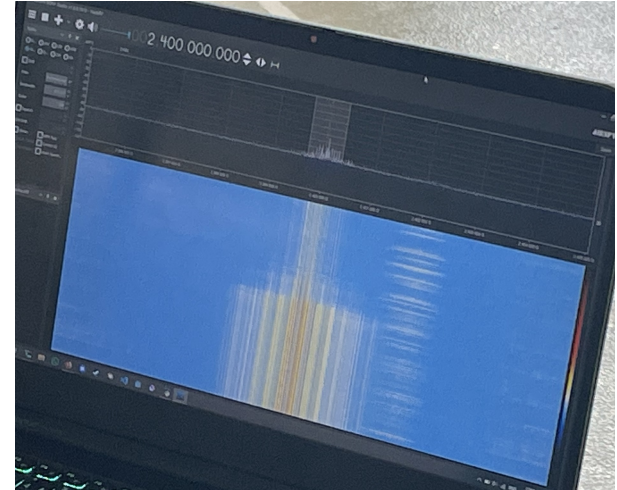
(a) $\theta = 0^\circ$ without IDC



(b) $\theta = 30^\circ$ without IDC



(c) $\theta = 60^\circ$ without IDC



(d) $\theta = 90^\circ$ without IDC

Figure 28: Waterfall diagrams without IDC. Peak signal strength is observed at $\theta = 0^\circ$, demonstrating forward radiation with no beam steering applied.

when a 0.52 radian phase shift was applied to a single element; later experimental testing confirmed this.

Still another crucial part focused on the design using interdigital capacitors of the phase-shifting mechanism. Their small form and simplicity of integration into the RF feed network guided IDCs to be chosen. IDC design drew on MATLAB's RF PCB Toolkit. Many geometrical parameters including number of fingers, finger length, spacing, and edge gap were optimized by a parametric sweep. After optimization, IDC is shown resonance at 2.4 GHz with an insertion phase of roughly 0.52 radian (30°). This matched the value required to point the beam of the array in the desired angle. The simulated S-parameters confirmed that the IDC reached a characteristic impedance of 50.88Ω and a return loss of -10.24 dB so guaranteeing suitable matching and minimum reflection losses.

Following successful stages of simulation and design, the project entered fabrication. We built both patch antennas and IDCs on a CNC3018 Pro PCB engraver. The fabrication process consisted in chemically etching the undesired copper using a hydrochloric acid and hydrogen peroxide mixture, engraving the feed and patch structures, and painting FR4 copper-clad boards. Selected based on dimensional compatibility with the intended feed structure, thinner and connected using RG58 coaxial cables helped to clean the final antennas. A Vector Network Analyzer (VNA) measured the made-up antennas. Good resonance characteristics within the 2.38–2.48 GHz range were confirmed by return loss curves for all four elements, which matched simulation data rather nicely.

The ITU Aerospace Research Center undertook experimental validation of the complete system. Two HackRF-

One software-defined radios—one serving as a transmitter and the other as a receiver—were built in a far-field test configuration. The 2×2 phased array was linked to the transmitting SDR, and a commercial dipole antenna linked the receiving SDR. The antennas were positioned 1.25 m apart, corresponding to 10 wavelengths at 2.4 GHz, to satisfy far field criteria. With and without the IDC in the system, the experiment consisted in rotating the antenna configuration to discrete angles of 0° , 30° , 60° and 90° . Each angle's received signal was tracked in real time using GNU Radio's waterfall diagram display.

The results of the measurements came clear. The array demonstrated peak reception at $\theta = 0^\circ$ without the IDC as would be expected from a symmetric, uniformly phased system. Following MATLAB array factor computations' theoretical prediction of $\theta = 33.5^\circ$ the reception peak shifted to $\theta = 30^\circ$ when the IDC was added into one element's feed line. These results provided strong evidence that the IDC effectively introduced the intended phase lag, so guiding the beam in the desired direction without active components. At the guided direction, the waterfall diagrams clearly showed higher spectral energy intensity and a corresponding decrease in power at non-optimal angles. Table 5 compares all design targets with simulation and measurement results.

Metric	Target	Simulation	Measurement
Resonant frequency (single patch) [GHz]	2.40	2.40	2.38–2.48
Resonant frequency (IDC) [GHz]	2.40	2.40	2.20–2.46
Beam-steering angle, θ_{\max} [deg]	30	33.5	30
IDC capacitance C [pF]	—	1.71	1.672
IDC insertion phase $\angle S_{21}$ @ 2.4 GHz [deg]	30	29.8	27.7
IDC input impedance Z_{in} [Ω]	50	50.9	55.8
IDC output impedance Z_{out} [Ω]	50	50.9	61.5

Table 5: Design targets compared with simulation and measurement

At last, this work demonstrates the feasibility and efficiency of using electronic beam steering in a planar phased array antenna system including passive components including interdigital capacitors. Together, analytical modeling, HFSS and MATLAB simulations, PCB-based fabrication, and empirical validation provides a whole end-to-end approach. Apart from proving passive beam steering, the project produced a modular and repeatable design framework. For applications in education, research, and prototyping, low-cost tools and readily available simulation tools help the approach to be feasible. The work informs future extensions including expansion to larger arrays with finer angular resolution, use of tunable dielectrics for real-time phase control, or 2D scanning through planar phase distribution. The outcomes confirm the pragmatic use of phased arrays in modern aircraft systems and provide a scalable path for next RF front-end design innovation.

For aviation platforms, the proposed passive-steered phased-array architecture provides a real operational benefit. The antenna system removes typically wear- or seizure-prone lubrication points, linkages, and bearings by substituting electronic beam steering based on interdigital capacitors for mechanically driven gimbals. Under vibration, temperature extremes, and pressure cycling typical of flight profiles, the absence of moving parts lowers unscheduled maintenance, increases mean time between failures (MTBF), and improves dispatch reliability. A conformal, low-profile array reduces structural protrusions and aerodynamic drag so enabling the antenna to be buried in radomes or skin panels without sacrificing fuel economy or radar signature.

Looking ahead, several technical benchmarks still stand. While the integration of barium-strontium-titanate (BST) coplanar-waveguide phase shifters will introduce dynamic, constantly variable steering rather than the present fixed 30° increases, scaling the array to a 4×4 (or larger) lattice will increase directivity and sharpen beam-width. Thermal cycling, vibration, humidity, and finally in-flight tests will validate long-term dependability and certify the design to RTCA DO-160 criteria. Concurrent work on conformal mounting techniques will investigate embedding the array into composite or metallic fuselage sections, so opening the path for really aerodynamic, maintenance-light communication and sensing solutions for next-generation aircraft.

VI. Acknowledgments

I would like to express my sincere gratitude to the ITU Aerospace Research Center for providing the facilities essential to this work, to Prof. Yeniçeri for his steadfast guidance throughout the year, and to my friend Aytaç Arıkan

for his invaluable insights and assistance during the testing phase. Finally, I extend my deepest thanks to my parents for their unwavering support over the course of my academic journey. Their encouragement has been instrumental in achieving the objectives of this project.

VII. References

- [1] R. L. Haupt and Y. Rahmat-Samii, “Antenna Array Developments: A Perspective on the Past, Present and Future,” *IEEE Antennas and Propagation Magazine*, vol. 57, no. 1, pp. 86–96, Feb. 2015, doi:10.1109/MAP.2015.2397154.
- [2] P. Rocca, N. Anselmi, M. A. Hannan, and A. Massa, “Modular Sparse Conical Multi-beam Phased Array Design for Air Traffic Control Radar,” arXiv:2108.08240 [eess.SP], 2021, doi:10.48550/arXiv.2108.08240.
- [3] M. Urcia and D. Banks, “Structurally integrated phased arrays,” in *Proc. 2011 Aerospace Conference*, Big Sky, MT, USA, 2011, pp. 1–8, doi:10.1109/AERO.2011.5747321.
- [4] S. Rao, A. Pandya, and C. Ostroot, “Phased Array Antennas For Aircraft Applications,” in *2018 IEEE Indian Conference on Antennas and Propagation (InCAP)*, Hyderabad, India, 2018, pp. 1–4, doi:10.1109/INCAP.2018.8770894.
- [5] M. T. Qureshi, V. Desmaris, M. Geurts, and J. van de Sluis, “Passive reciprocal high-pass/low-pass 4-bit phase shifter at 2.45 GHz,” in *2014 44th European Microwave Conference*, Rome, Italy, 2014, pp. 1076–1078, doi:10.1109/EuMC.2014.6986625.
- [6] T. A. P. Agung and J. Suryana, “Design and realization of passive phase shifter for non mechanical 1.8 GHz BTS antenna tilting,” in *2012 7th International Conference on Telecommunication Systems, Services, and Applications (TSSA)*, Denpasar-Bali, Indonesia, 2012, pp. 223–226, doi:10.1109/TSSA.2012.6366056.
- [7] S. Ganjeheizadeh Rohani, *Printed planer phase shifters for phased array antennas*, Ph.D. dissertation, ProQuest Dissertations and Theses Global, no. 28087446, 2020. Available: <https://www.proquest.com/dissertations-theses/printed-planar-phase-shifters-phased-array/docview/2446959524/se-2>.
- [8] ANSYS, Inc., *ANSYS HFSS (Version 2022 R2)* [Computer software], Canonsburg, PA, USA, 2024. Available: <https://www.ansys.com/>.
- [9] The MathWorks, Inc., *MATLAB (Version R2022b)* [Computer software], Natick, MA, USA, 2024. Available: <https://www.mathworks.com>.
- [10] C. A. Balanis, *Antenna Theory: Analysis and Design*, 4th ed. Hoboken, NJ: John Wiley Sons, 2016.
- [11] I. Bahl, *Lumped Elements for RF and Microwave Circuits*. Norwood, MA: Artech House, 2003.
- [12] R. J. Mailloux, *Phased Array Antenna Handbook*, 2nd ed. Norwood, MA: Artech House, 2005.
- [13] Z. Cao, F. Li, H. P. A. van den Boom, E. Tangdiongga, and A. M. J. Koonen, “Optical true-time-delay microwave beam-steering with 1 Gb/s wireless transmission for in-building networks,” in *Proc. 39th European Conference and Exhibition on Optical Communication (ECOC 2013)*, London, UK, 2013, pp. 1–3, doi:10.1049/cp.2013.1353.
- [14] K. Liu, X. Guo, T. Liu, and W. Wang, “Design, Fabrication, and Measurement Study of a Planar Phased Array Antenna,” *IEEE Transactions on Instrumentation and Measurement*, vol. 72, pp. 1–9, 2023, Art. no. 1007509, doi:10.1109/TIM.2023.3296129.

VIII. Appendicies

A. Project Schedule

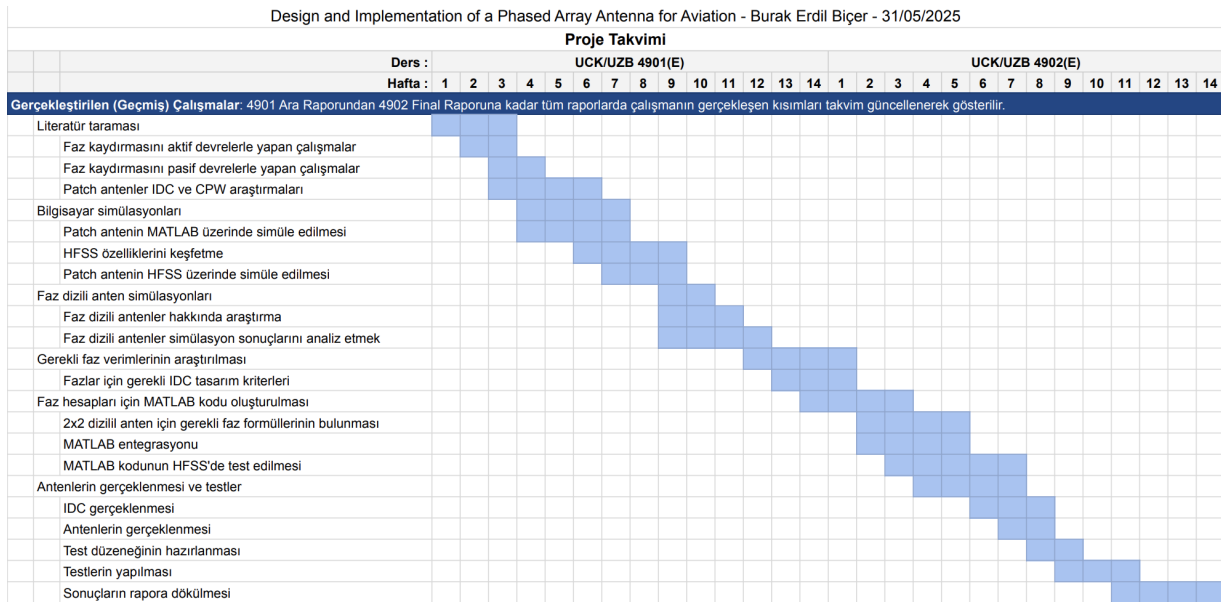


Figure 29: Project schedule provided for every week.

B. Statement of Ethics

Each aspect of this project was finished responsibly and honestly. Author using reliable tools like MATLAB and ANSYS HFSS conducted the simulations, computations, and tests. Not one bit of information or data was altered or added in. Every source and reference applied in the project has been precisely noted. Under consideration the need of safety and accuracy in aviation systems, the work was done with respect for academic rules and engineering ethics.

C. MATLAB Codes

```

1 % inputs: scan frequency and angles
2 ScanFrequency = 2.4e9;           % frequency in Hz
3 ScanAngleTheta = pi/4;          % angle in radians
4 ScanAnglePhi   = pi/6;          % angle in radians
5 ScanPhase1     = 0;              % base phase
6
7 % computation
8 % Compute ScanPhaseShiftA and ScanPhaseShiftB
9 ScanPhaseShiftA = -((ScanFrequency * 0.0 * sin(ScanAngleTheta) * cos(ScanAnglePhi)
10 ) + ...
11             (ScanFrequency * 2.69525669823e-09 * sin(ScanAngleTheta) * sin(
12                 ScanAnglePhi)));
13 ScanPhaseShiftB = -((ScanFrequency * 1.40421616471e-09 * sin(ScanAngleTheta) * cos(
14                 ScanAnglePhi)) + ...
15             (ScanFrequency * 0.0 * sin(ScanAngleTheta) * sin(ScanAnglePhi))
16 );
17
18 % Convert to degrees
19 ScanPhaseShiftA_deg = rad2deg(ScanPhaseShiftA);

```

```

16 ScanPhaseShiftB_deg = rad2deg(ScanPhaseShiftB);
17
18 % Display
19 disp('ScanPhaseShiftA (Radians):'), disp(ScanPhaseShiftA)
20 disp('ScanPhaseShiftA (Degrees):'), disp(ScanPhaseShiftA_deg)
21 disp('ScanPhaseShiftB (Radians):'), disp(ScanPhaseShiftB)
22 disp('ScanPhaseShiftB (Degrees):'), disp(ScanPhaseShiftB_deg)
23
24 % Define the antenna array dimensions
25 rows = 2;
26 cols = 2;
27
28 % Initialize phase matrices
29 Phases_rad = zeros(rows, cols);
30 Phases_deg = zeros(rows, cols);
31
32 % Compute the phase for each antenna element
33 for i = 1:rows
34     for j = 1:cols
35         Phases_rad(i,j) = ScanPhase1 + ((i-1) * ScanPhaseShiftA + (j-1) *
36             ScanPhaseShiftB);
37         Phases_deg(i,j) = rad2deg(Phases_rad(i,j));
38     end
39 end
40
41 % Display results
42 disp('Antenna Element Phases (Radians):')
43 disp(Phases_rad)
44 disp('Antenna Element Phases (Degrees):')
45 disp(Phases_deg)

```

Listing 1: MATLAB code to calculate required phase shifts

```

1 Phases_rad = [ 0.52, 0;          % row 1: element (1,1), (1,2)
2                 0, 0];          % row 2: element (2,1), (2,2)
3
4 ScanFrequency = 2.4e9;           % Hz
5 dt_x = 1.40421616471e-9;       % inter-element time delay in x (sec)
6 dt_y = 2.69525669823e-9;       % inter-element time delay in y (sec)
7 c = 3e8;                        % m/s
8 lambda = c/ScanFrequency;
9 k = 2*pi/lambda;
10
11 % --- Scan grid for (theta, phi) ---
12 theta_vec = linspace(0,pi/2,181);    % 0      90      in 0.5   steps
13 phi_vec   = linspace(0,2*pi,361);    % 0      360     in 1    steps
14
15 AF = zeros(length(theta_vec), length(phi_vec)); % array factor
16
17 % --- Compute array factor over the grid ---
18 for ti = 1:length(theta_vec)
19     th = theta_vec(ti);
20     for pi = 1:length(phi_vec)
21         ph = phi_vec(pi);
22         % for each element (i,j) compute its extra phase due to direction:
23         psi = zeros(2,2);
24         for i = 1:2
25             for j = 1:2
26                 % spatial phase term = k*( x*sin    cos    + y*sin    sin    )

```

```

27         x = (j-1)*(dt_x * c);
28         y = (i-1)*(dt_y * c);
29         psi(i,j) = k*( x*sin(th)*cos(ph) + y*sin(th)*sin(ph) );
30     end
31 end
32 % total AF = sum over elements of exp[j*(appliedPhase + spatialPhase)]
33 AF(ti,pi) = sum( sum( exp(1j*(Phases_rad + psi)) ) );
34 end
35 end
36
37 % --- Find peak of |AF| and report its angles ---
38 [~, idx] = max(abs(AF(:)));
39 [ti_opt, pi_opt] = ind2sub(size(AF), idx);
40 theta_opt = theta_vec(ti_opt);
41 phi_opt = phi_vec(pi_opt);
42
43 fprintf('Beam maximum at Theta = %.2f \n', rad2deg(theta_opt));
44 fprintf('Beam maximum at Phi = %.2f \n', rad2deg(phi_opt));

```

Listing 2: MATLAB code used to compute the resulting beam direction of a 2x2 phased array antenna based on manually applied phase values and spatial scanning over (θ, ϕ) space. The array factor is evaluated to identify the peak direction in the far field.

```

1 clear; clc;
2 %% 1. Substrate and metal
3 sub = dielectric( ...
4     "Name" , "FR4" , ...
5     "EpsilonR" , 4.4 , ... % nominal r
6     "LossTangent" , 0.02 , ... % FR-4 loss
7     "Thickness" , 1.6e-3); % 1.6 mm board
8 cu = metal("Copper"); % default: 5 m thick
9
10 %% 2. Parameter grids
11 Lvec = 20e-3 : 5e-3 : 25e-3; % finger length sweep (20 25 mm in 5 mm steps)
12 Nvec = 4 : 4 : 8; % number of fingers sweep (4 or 8)
13 gap = 0.5e-3;
14 w = 0.5e-3;
15 f0 = 2.4e9;
16 nofpoints = 200;
17
18 %% 3. IDC-specific parameters
19 fingerspacing = 0.5e-3;
20 portwidth = 3.0e-3;
21 groundwidth = 0.01;
22
23 %% 4. Initial parametric sweep
24 best.err = inf;
25 for L = Lvec
26     for N = Nvec
27         IDC = interdigitalCapacitor( ...
28             "NumFingers" , N, ...
29             "FingerLength" , L, ...
30             "FingerWidth" , w, ...
31             "FingerSpacing" , fingerspacing, ...
32             "FingerEdgeGap" , gap, ...
33             "PortLineWidth" , portwidth, ...
34             "GroundPlaneWidth" , groundwidth, ...
35             "Substrate" , sub, ...

```

```

37     "Conductor"      , cu);
38 S = sparameters(IDC, linspace(2e9,2.8e9,nofpoints));
39 S11 = squeeze(S.Parameters(1,1,:));
40 [~,idx] = min(abs(S11));
41 fres = S.Frequencies(idx);
42 err = abs(fres - f0);
43 if err < best.err
44     best.err = err;
45     best.L = L;
46     best.N = N;
47     best.fres = fres;
48     best.S = S;
49 end
50 end
51 end
52
53 fprintf('Initial best: L = %.2f mm, N = %d      fres = %.3f GHz\n', ...
54         best.L*1e3, best.N, best.fres/1e9);
55
56 %% 5. Iterative tuning using scaling laws
57 maxIter = 5;
58 tol = 1e6;    % tolerance in Hz
59 L_curr = best.L;
60 N_curr = best.N;
61 f_curr = best.fres;
62
63 for iter = 1:maxIter
64     % compute scaled geometry
65     L_new = L_curr * (f_curr/f0)^2;
66     Nf = (N_curr-1) * (f_curr/f0)^2 + 1;
67     N_new = max(2, round(Nf));    % ensure at least 2 fingers
68
69     % build and evaluate new IDC
70     IDCt = interdigitalCapacitor( ...
71         "NumFingers"      , N_new, ...
72         "FingerLength"    , L_new, ...
73         "FingerWidth"     , w, ...
74         "FingerSpacing"   , fingerspacing, ...
75         "FingerEdgeGap"   , gap, ...
76         "PortLineWidth"   , portwidth, ...
77         "GroundPlaneWidth", groundwidth, ...
78         "Substrate"        , sub, ...
79         "Conductor"        , cu);
80     St = sparameters(IDCt, linspace(2e9,2.8e9,nofpoints));
81     S11t = squeeze(St.Parameters(1,1,:));
82     [~,idxt] = min(abs(S11t));
83     f_new = St.Frequencies(idxt);
84     err_new = abs(f_new - f0);
85
86     fprintf('Iter %d: L=% .2f mm, N=%d      fres=% .3f GHz, err=% .1f MHz\n', ...
87             iter, L_new*1e3, N_new, f_new/1e9, err_new/1e6);
88
89     % check convergence
90     if err_new < tol
91         L_curr = L_new;
92         N_curr = N_new;
93         f_curr = f_new;
94         break;
95 end

```

```

96 % update for next iteration
97 L_curr = L_new;
98 N_curr = N_new;
99 f_curr = f_new;
100 end
101
102 fprintf('Final tuned: L = %.2f mm, N = %d      fres = %.3f GHz\n', ...
103     L_curr*1e3, N_curr, f_curr/1e9);
104
105 %% 6. Display tuned geometry and response
106 IDCtuned = interdigitalCapacitor( ...
107     "NumFingers" , N_curr, ...
108     "FingerLength" , L_curr, ...
109     "FingerWidth" , w, ...
110     "FingerSpacing" , fingerspacing, ...
111     "FingerEdgeGap" , gap, ...
112     "PortLineWidth" , portwidth, ...
113     "GroundPlaneWidth", groundwidth, ...
114     "Substrate" , sub, ...
115     "Conductor" , cu);
116 figure; show(IDCtuned); title("Tuned IDC geometry");
117 figure; rfplot(St); xlim([2 3]); grid on; title("S_{11} after tuning");
118
119 %% 7. Characteristic impedance
120 txl = txlineMicrostrip( ...
121     "Width" , portwidth, ...
122     "Height" , sub.Thickness, ...
123     "Thickness" , cu.Thickness, ...
124     "EpsilonR" , sub.EpsilonR, ...
125     "SigmaCond" , cu.Conductivity);
126 Z0_f = getZ0(txl, f0); % Z0 at f0 : contentReference[oaicite:1]{index=1}
127 fprintf("Characteristic impedance at %.2f GHz: %.2f + %.2fi \n", f0/1e9, real(
    Z0_f), imag(Z0_f));

```

Listing 3: MATLAB code to calculate simulate and optimize the IDC.